Influence of nonlocal damping on magnon properties of ferromagnets

Zhiwei Lu,[1,*,†] I. P. Miranda,[2,*] Simon Streib,[2] Manuel Pereiro,[2] Erik Sjöqvist,[2] Olle Eriksson,[2,3] Anders Bergman,[2] Danny Thonig,[3,2] and Anna Delin[1,4]

[1]*Department of Applied Physics, School of Engineering Sciences, KTH Royal Institute of Technology, AlbaNova University Center, SE-10691 Stockholm, Sweden*

[2]*Department of Physics and Astronomy, Uppsala University, Box 516, SE-75120 Uppsala, Sweden*

[3]*School of Science and Technology, Örebro University, SE-701 82 Örebro, Sweden*

[4]*SeRC (Swedish e-Science Research Center), KTH Royal Institute of Technology, SE-10044 Stockholm, Sweden*

(Received 24 November 2022; revised 8 May 2023; accepted 14 July 2023; published 28 July 2023)

We study the influence of nonlocal damping on the magnon properties of Fe, Co, Ni, and $Fe_{1-x}Co_x$ ($x = 30\%, 50\%$) alloys. The Gilbert damping parameter is typically considered as a local scalar both in experiment and in theoretical modeling. However, recent works have revealed that Gilbert damping is a nonlocal quantity that allows for energy dissipation between atomic sites. With the Gilbert damping parameters calculated from a state-of-the-art real-space electronic structure method, magnon lifetimes are evaluated from spin dynamics and linear response, where a good agreement is found between these two methods. It is found that nonlocal damping affects the magnon lifetimes in different ways depending on the system. Specifically, we find that in Fe, Co, and Ni, the nonlocal damping decreases the magnon lifetimes, while in $Fe_{70}Co_{30}$ and $Fe_{50}Co_{50}$ an opposite, nonlocal damping effect is observed, and our data show that it is much stronger in the former.

DOI: 10.1103/PhysRevB.108.014433

I. INTRODUCTION

In recent years, there has been a growing interest in magnonics, which uses quasiparticle excitations in magnetically ordered materials to perform information transport and processing on the nanoscale. Compared with conventional information-technology devices, magnonics-based devices exhibit lower energy consumption, easier integrability with complementary metal-oxide semiconductor (CMOS) structures, anisotropic properties, and efficient tunability by various external stimuli, to name a few [1–10]. Yttrium iron garnet (YIG) [11] as well as other iron garnets with rare-earth elements (Tm, Tb, Dy, Ho, Er) [12] are very promising candidates for magnonics-based device applications due to their low-energy dissipation properties and thus long spin-wave propagation distances up to tens of μm. In contrast, the damping in other materials relevant for magnonics, such as CoFeB, is typically two orders of magnitude higher compared with YIG [12], leading to much shorter spin-wave propagation distances. A clear distinction can be made between materials with an ultralow damping parameter, such as YIG, and those with a significantly larger, but still small, damping parameter. In materials that are insulating, such as YIG, many of the microscopic mechanisms responsible for damping are hindered, resulting in the low observed damping parameter. In contrast, materials such as CoFeB are metallic. In research projects that utilize low damping materials, YIG and similar nonmetallic low damping systems are typically favored. However, metallic systems have an advantage, since magnetic textures can easily be influenced by electrical currents. Hence, there is good reason to consider metallic systems for low damping applications, even though their damping is typically larger than in YIG. One can conclude that Gilbert damping is one of the major bottlenecks for the choice of material in magnonics applications, and a detailed experimental as well as theoretical characterization is fundamental for this field of research, especially for metallic systems. Thus, a more advanced and detailed understanding of Gilbert damping is called for in order to overcome this obstacle for further development of magnonics-based technology.

Whereas most studies consider chemical modifications of the materials in order to tune the damping [13,14], only a few focus on the fundamental physical properties as well as dependencies of the Gilbert damping. Often, Gilbert damping is considered to be a phenomenological scalar parameter in the equation of motion of localized atomistic magnetic moments, i.e., the Landau-Lifshitz-Gilbert (LLG) equation [15]. However, from using the general Rayleigh dissipation function in the derivation proposed by Gilbert [16], it was theoretically found that the Gilbert damping should be anisotropic, a tensor, and nonlocal, especially in some low symmetric systems. Furthermore, it depends on the temperature and thus on the underlying magnon as well as phonon configurations [17–20]. This is naturally built into the multiple theoretical methods

*These authors contributed equally to this work.
†Corresponding author: zhiweil@kth.se

developed to predict the damping parameter, including the breathing Fermi surface model [21], the torque correlation model [22], and the linear-response formulation [23]. For instance, the general Gilbert damping tensor as a function of the noncollinear spin configuration has been proposed in Ref. [24].

Nonetheless, an experimental verification is still missing due to lacking insights into the impact of the generalized damping on experimental observables. Changes of Gilbert damping in a magnetic domain wall, and thus its dependency on the magnetic configuration, were measured in Ref. [25] and fitted to the Landau-Lifshitz-Baryakhtar (LLBar) equation, which includes nonlocality of the damping by an additional dissipation term proportional to the gradient of the magnetization [26–28]. However, the pairwise nonlocal damping α_{ij} has not yet been measured.

The most common experimental techniques of evaluating damping are ferromagnetic resonance (FMR) [29] and the time-resolved magneto-optical Kerr effect (TR-MOKE) [30]. In these experiments, Gilbert damping is related to the relaxation rate (i) when slightly perturbing the coherent magnetic moment out of equilibrium by an external magnetic field [31], or (ii) when disordered magnetic moments remagnetize after pumping by an ultrafast laser pulse [32]. Normally, in case (i) the nonlocality is suppressed due to the coherent precession of the atomic magnetic moments. However, this coherence can be perturbed by temperature, making nonlocality in principle measurable. One possible other path to link nonlocal damping with experiment is magnon lifetimes. Theoretically, the magnon properties as well as the impact of damping on these properties can be assessed from the dynamical structure factor, and atomistic spin-dynamics simulations have been demonstrated to yield magnon dispersion relations that are in good agreement with experiment [33]. In experiment, neutron scattering [34] and electron scattering [35] are the most common methods for probing magnon excitations, where the linewidth broadening of magnon excitations is related to damping and provides a way to evaluate the magnon lifetimes [36]. It is found in ferromagnets that the magnon lifetimes are wave-vector (magnon-energy) -dependent [37–39]. It has been reported that the magnon energy in Co films is nearly twice as large as in Fe films, but they have similar magnon lifetimes, which is related to the intrinsic damping mechanism of materials [40]. However, this collective effect of damping and magnon energy on magnon lifetimes is still an open question. The study of this collective effect is of great interest for both theory and device applications.

Here, we report an implementation for solving the stochastic Landau-Lifshitz-Gilbert (SLLG) equation incorporating the nonlocal damping. With the dynamical structure factor extracted from the spin-dynamics simulations, we investigate the collective effect of nonlocal damping and magnon energy on the magnon lifetimes. We propose an efficient method to evaluate magnon lifetimes from linear-response theory, and we verify its validity.

The paper is organized as follows. In Sec. II, we give the simulation details of the spin dynamics, the adiabatic magnon spectra and dynamical structure factor, and the methodology of DFT calculations and linear response. Section III presents the nonlocal damping in real-space, nonlocal damping effects on the spin dynamics and magnon properties including magnon lifetimes of pure ferromagnets (Fe,Co,Ni), and $Fe_{1-x}Co_x$ ($x = 30\%, 50\%$) alloys. In Sec. IV, we provide a summary and an outlook.

II. THEORY

A. Nonlocal damping in atomistic spin dynamics

The dynamical properties of magnetic materials at finite temperature have been simulated up to now from atomistic spin dynamics by means of the stochastic Landau-Lifshitz-Gilbert (SLLG) equation with scalar local energy dissipation. Here, the time evolution of the magnetic moments $\boldsymbol{m}_i = m_i \boldsymbol{e}_i$ at atom site i is well described by

$$\frac{\partial \boldsymbol{m}_i}{\partial t} = \boldsymbol{m}_i \times \left(-\gamma [\boldsymbol{B}_i + \boldsymbol{b}_i(t)] + \frac{\alpha}{m_i} \frac{\partial \boldsymbol{m}_i}{\partial t} \right), \tag{1}$$

where γ is the gyromagnetic ratio. The effective field $\boldsymbol{B}_i$ acting on each magnetic moment is obtained from

$$\boldsymbol{B}_i = -\frac{\partial \mathcal{H}}{\partial \boldsymbol{m}_i}. \tag{2}$$

The spin-Hamiltonian $\mathcal{H}$ considered here consists of a Heisenberg spin-spin exchange:

$$\mathcal{H} = -\frac{1}{2} \sum_{i \neq j} J_{ij} \boldsymbol{e}_i \cdot \boldsymbol{e}_j. \tag{3}$$

Here, J_{ij}—the Heisenberg exchange parameter—couples the spin at site i with the spin at site j and is calculated from first principles (see Sec. II C). Furthermore, α is the scalar phenomenological Gilbert damping parameter. Finite temperature T is included in Eq. (1) via the fluctuating field $\boldsymbol{b}_i(t)$, which is modeled by uncorrelated Gaussian white noise: $\langle \boldsymbol{b}_i(t) \rangle = 0$ and $\langle b_i^\mu(t) b_j^\nu(t') \rangle = 2D\delta_{ij}\delta_{\mu\nu}\delta(t-t')$, where δ is the Kronecker delta, i, j are site indices, and μ, $\nu = \{x, y, z\}$ are Cartesian indices. Furthermore, the fluctuation-dissipation theorem gives $D = \alpha \frac{k_B T}{\gamma m_i}$ (see, e.g., Ref. [41]), with the Boltzmann constant k_B.

A more generalized form of the SLLG equation that includes nonlocal tensorial damping has been reported in previous studies [20,42,43] and is

$$\frac{\partial \boldsymbol{m}_i}{\partial t} = \boldsymbol{m}_i \times \left(-\gamma [\boldsymbol{B}_i + \boldsymbol{b}_i(t)] + \sum_j \frac{\alpha_{ij}}{m_j} \frac{\partial \boldsymbol{m}_j}{\partial t} \right), \tag{4}$$

which can be derived from the Rayleigh dissipation functional in the Lagrange formalism used by Gilbert [16]. In the presence of nonlocal damping, the Gaussian fluctuating field fulfills [42,44,45]

$$\left\langle b_i^\mu(t) b_j^\nu(t') \right\rangle = 2D_{ij}^{\mu\nu}\delta(t-t'), \tag{5}$$

with $D_{ij}^{\mu\nu} = \alpha_{ij}^{\mu\nu} \frac{k_B T}{\gamma m_i}$. The damping tensor $\alpha_{ij}^{\mu\nu}$ must be positive-definite in order to be physically defined. Along with spatial nonlocality, the damping can also be nonlocal in time, as discussed in Ref. [46]. To prove the fluctuation-dissipation theorem in Eq. (5), the Fokker-Planck equation has to be analyzed in the presence of nonlocal damping, similar to Ref. [15]. This is, however, not the purpose of this paper. Instead, we will use the approximation $\alpha_{ij}^{\mu\nu} = \frac{1}{3}\mathrm{Tr}\{\alpha_{ii}\}\delta_{\mu\nu}$

within the diffusion constant $D_{ij}^{\mu\nu}$. Such an approximation is strictly valid only in the low-temperature limit.

To solve this SLLG equation incorporating the nonlocal damping, we have implemented an implicit midpoint solver in the UPPASD code [47]. This iterative fix-point scheme converges within an error of $10^{-10}\mu_B$, which is typically equivalent to six iteration steps. More details of this solver are provided in Appendix A. The initial spin configuration in the typical $N = 20 \times 20 \times 20$ supercell with periodic boundary conditions starts from a totally random state. The spin-spin exchange interactions and nonlocal damping parameters are included up to at least 30 shells of neighbors in order to guarantee the convergence with respect to the spatial expansion of these parameters (a discussion about the convergence is given in Sec. III A). Observables from our simulations are typically the average magnetization $\boldsymbol{M} = \frac{1}{N}\sum_i^N \boldsymbol{m}_i$ as well as the magnon dispersion.

B. Magnon dispersion

Two methods to simulate the magnon spectrum are applied in this paper: (i) the dynamical structure factor, and (ii) the frozen magnon approach.

For the dynamical structure factor $S(\boldsymbol{q}, \omega)$ at finite temperature and damping [33,48], the spatial and time correlation function between two magnetic moments i at position $\boldsymbol{r}$ and j at position $\boldsymbol{r}'$ as well as different times 0 and t is expressed as

$$C^{\mu}(\boldsymbol{r}-\boldsymbol{r}', t) = \left\langle m_{\boldsymbol{r}}^{\mu}(t) m_{\boldsymbol{r}'}^{\mu}(0)\right\rangle - \left\langle m_{\boldsymbol{r}}^{\mu}(t)\right\rangle\left\langle m_{\boldsymbol{r}'}^{\mu}(0)\right\rangle. \quad (6)$$

Here $\langle\cdot\rangle$ denotes the ensemble average, and μ are Cartesian components. The dynamical structure factor can be obtained from the time and space Fourier transform of the correlation function, namely

$$S^{\mu}(\boldsymbol{q}, \omega) = \frac{1}{\sqrt{2\pi}N}\sum_{\boldsymbol{r},\boldsymbol{r}'} e^{i\boldsymbol{q}\cdot(\boldsymbol{r}-\boldsymbol{r}')}\int_{-\infty}^{\infty} e^{i\omega t} C^{\mu}(\boldsymbol{r}-\boldsymbol{r}', t)dt. \quad (7)$$

The magnon dispersion is obtained from the peak positions of $S(\boldsymbol{q}, \omega)$ along different magnon wave vectors $\boldsymbol{q}$ in the Brillouin zone and magnon energies ω. It should be noted that $S(\boldsymbol{q}, \omega)$ is related to the scattering intensity in inelastic neutron scattering experiments [49]. The broadening of the magnon spectrum correlates with the lifetime of spin waves mediated by Gilbert damping as well as intrinsic magnon-magnon scattering processes. Good agreement between $S(\boldsymbol{q}, \omega)$ and experiment has been found previously [33].

The second method—the frozen magnon approach—determines the magnon spectrum directly from the Fourier transform of the spin-spin exchange parameters J_{ij} [50,51] and nonlocal damping α_{ij}. At zero temperature, a time-dependent external magnetic field is considered,

$$B_i^{\pm}(t) = \frac{1}{N}\sum_{\boldsymbol{q}} B_{\boldsymbol{q}}^{\pm} e^{i\boldsymbol{q}\cdot\boldsymbol{R}_i - i\omega t}, \quad (8)$$

where N is the total number of lattice sites and $B_{\boldsymbol{q}}^{\pm} = B_{\boldsymbol{q}}^{x} \pm iB_{\boldsymbol{q}}^{y}$. The linear response to this field is then given by

$$M_{\boldsymbol{q}}^{\pm} = \chi^{\pm}(\boldsymbol{q}, \omega) B_{\boldsymbol{q}}^{\pm}. \quad (9)$$

We obtain for the transverse dynamic magnetic susceptibility [52,53]

$$\chi^{\pm}(\boldsymbol{q}, \omega) = \frac{\pm\gamma M_s}{\omega \pm \omega_{\boldsymbol{q}} \mp i\omega\alpha_{\boldsymbol{q}}}, \quad (10)$$

with saturation magnetization M_s, spin-wave frequency $\omega_{\boldsymbol{q}} = E(\boldsymbol{q})/\hbar$, and damping

$$\alpha_{\boldsymbol{q}} = \sum_j \alpha_{0j} e^{-i\boldsymbol{q}\cdot(\boldsymbol{R}_0 - \boldsymbol{R}_j)}. \quad (11)$$

We can extract the spin-wave spectrum from the imaginary part of the susceptibility,

$$\mathrm{Im}\chi^{\pm}(\boldsymbol{q}, \omega) = \frac{\gamma M_s \alpha_{\boldsymbol{q}}\omega}{[\omega \pm \omega_{\boldsymbol{q}}]^2 + \alpha_{\boldsymbol{q}}^2\omega^2}, \quad (12)$$

which is equivalent to the correlation function $S^{\pm}(\boldsymbol{q}, \omega)$ due to the fluctuation-dissipation theorem [54]. We find that the spin-wave lifetime $\tau_{\boldsymbol{q}}$ is determined by the Fourier transform of the nonlocal damping (for $\alpha_{\boldsymbol{q}} \ll 1$),

$$\tau_{\boldsymbol{q}} = \frac{\pi}{\alpha_{\boldsymbol{q}}\omega_{\boldsymbol{q}}}. \quad (13)$$

The requirement of positive-definiteness of the damping matrix α_{ij} directly implies $\alpha_{\boldsymbol{q}} > 0$, since α_{ij} is diagonalized by Fourier transformation due to translational invariance. Hence, $\alpha_{\boldsymbol{q}} > 0$ is a criterion to evaluate whether the damping quantity in real space is physically consistent and whether first-principles calculations are well converged. If $\alpha_{\boldsymbol{q}} < 0$ for some wave vector $\boldsymbol{q}$, energy is pumped into the spin system at the corresponding magnon mode, preventing the system from fully reaching the saturation magnetization at sufficiently low temperatures.

The effective damping α_0 of the FMR mode at $\boldsymbol{q} = \boldsymbol{0}$ is determined by the sum over all components of the damping matrix, following Eq. (11),

$$\alpha_{\mathrm{tot}} \equiv \alpha_0 = \sum_j \alpha_{0j}. \quad (14)$$

Therefore, an effective local damping should be based on α_{tot} if the full nonlocal damping is not taken into account.

C. Details of the DFT calculations

The electronic structure calculations, in the framework of density functional theory (DFT), were performed using the fully self-consistent real-space linear muffin-tin orbital in the atomic sphere approximation (RS-LMTO-ASA) [55,56]. The RS-LMTO-ASA uses the Haydock recursion method [57] to solve the eigenvalue problem based on a Green's functions methodology directly in real space. In the recursion method, the continued fractions have been truncated using the Beer-Pettifor terminator [58], after a number LL of recursion levels. The LMTO-ASA [59] is a linear method that gives precise results around an energy E_v, usually taken as the center of the s, p, and d bands. Therefore, as we calculate fine quantities as the nonlocal damping parameters, we consider here an expression accurate to $(E - E_v)^2$ starting from the orthogonal representation of the LMTO-ASA formalism [60].

For bcc FeCo alloys and bcc Fe, we considered $LL = 31$, while for fcc Co and fcc Ni much higher LL values (51 and

47, respectively) are needed to better describe the density of states and Green's functions at the Fermi level.

The spin-orbit coupling (SOC) is included as an $l \cdot s$ [59] term computed in each variational step [61]. All calculations were performed within the local spin density approximation (LSDA) exchange-functional (XC) by von Barth and Hedin [62], as it gives general magnetic information with equal or better quality than, e.g., the generalized gradient approximation (GGA). Indeed, the choice of XC between LSDA and GGA [63] has a minor impact on the on-site damping and the shape of the $\alpha_{\boldsymbol{q}}$ curves, as well as the analyzed properties (remagnetization, magnon lifetimes) when considering the same lattice parameters (data not shown). No orbital polarization [64] was considered here. Each bulk system was modeled by a big cluster containing ∼55 000 (bcc) and ∼696 000 (fcc) atoms located in the perfect crystal positions with the respective lattice parameters of $a = 2.87$ Å (bcc Fe and bcc $Fe_{1-x}Co_x$, sufficiently close to experimental observations [65]), $a = 3.54$ Å (fcc Co [20,66]), and $a = 3.52$ Å (fcc Ni [67]). To account for the chemical disorder in the $Fe_{70}Co_{30}$ and $Fe_{50}Co_{50}$ bulk systems, the electronic structure was calculated within the simple virtual-crystal approximation (VCA), which has been shown to work well for the ferromagnetic transition-metal alloys (particularly for elements next to each other in the Periodic Table, such as FeCo and CoNi) [68–75], and it is also described as being in good agreement with the damping trends in both FeCo and CoNi (see Appendix C). However, it is known that VCA neglects both short-range-order effects and scattering of electrons caused by the random distribution of atoms in the system, while the latter is better treated by the coherent-potential approximation (CPA) [76,77]. Despite these limitations, VCA is a computationally efficient scheme also for the real-space DFT method applied here, which otherwise entails computationally demanding alloying over thousands of samples.

As reported in Ref. [78], the total damping of site i, influenced by the interaction with neighbors j, can be decomposed in two main contributions: The on-site contribution (for $i = j$), and the nonlocal contribution (for $i \neq j$). Both can be calculated, in the collinear framework, by the following expression:

$$\alpha_{ij}^{\mu\nu} = \alpha_C \int_{-\infty}^{\infty} \eta(\epsilon) \mathrm{Tr}\left(\hat{T}_i^{\mu} \hat{A}_{ij} \left(\hat{T}_j^{\nu}\right)^{\dagger} \hat{A}_{ji}\right) d\epsilon \xrightarrow{T \to 0\,\mathrm{K}} \times \alpha_C \mathrm{Tr}\left(\hat{T}_i^{\mu} \hat{A}_{ij}(\epsilon_F + i\delta) \left(\hat{T}_j^{\nu}\right)^{\dagger} \hat{A}_{ji}(\epsilon_F + i\delta)\right), \quad (15)$$

where we define $\hat{A}_{ij}(\epsilon + i\delta) = \frac{1}{2i}[\hat{G}_{ij}(\epsilon + i\delta) - \hat{G}_{ji}^{\dagger}(\epsilon + i\delta)]$ as the anti-Hermitian part of the retarded physical Green's functions in the LMTO formalism, and $\alpha_C = \frac{g}{m_{t_i}\pi}$ is a prefactor related to the ith site magnetization. The imaginary part, δ, is obtained from the terminated continued fractions in the present calculations [58]. Also in Eq. (15), $\hat{T}_i^{\mu} = [\sigma_i^{\mu}, \mathcal{H}_{\mathrm{SO}_i}]$ is the so-called torque operator [20] evaluated in each Cartesian direction $\mu, \nu = \{x, y, z\}$ at site i, $\eta(\epsilon) = -\frac{\partial f(\epsilon)}{\partial \epsilon}$ is the derivative of the Fermi-Dirac distribution $f(\epsilon)$ with respect to the energy ϵ, $g = 2(1 + \frac{m_{\mathrm{orb}}}{m_{\mathrm{spin}}})$ is the g-factor (not considering here the spin-mixing parameter [79]), σ^{μ} are the Pauli matrices, and m_{t_i} is the total magnetic moment of site i ($m_{t_i} = m_{\mathrm{orb}_i} + m_{\mathrm{spin}_i}$). This results in a 3×3 tensor with terms $\alpha_{ij}^{\mu\nu}$. In the real-space bulk calculations performed in the present work, the α_{ij} (with $i \neq j$) matrices contain off-diagonal terms that are canceled by the summation of the contributions of all neighbors within a given shell, resulting in a purely diagonal damping tensor, as expected for symmetry reasons [15]. Therefore, as in the DFT calculations the spin quantization axis is considered to be in the z ([001]) direction (collinear model), we can ascribe a scalar damping value α_{ij} as the average $\alpha_{ij} = \frac{1}{2}(\alpha_{ij}^{xx} + \alpha_{ij}^{yy}) = \alpha_{ij}^{xx}$ for the systems investigated here. This scalar α_{ij} is then used in the SLLG equation [Eq. (1)]. In the above demonstrated torque-torque correlation method, only the spin-orbit induced torque is considered. Turek *et al.* [77] and Garate *et al.* [80] have shown that the use of the complete torque, including torque induced by the local spin-dependent exchange-correlation potential and by the spin-orbit coupling, leads to an identically zero result.

The exchange parameters J_{ij} in the Heisenberg model were calculated by the Liechtenstein-Katsnelson-Antropov-Gubanov (LKAG) formalism [81], according to the implementation in the RS-LMTO-ASA method [60]. Hence all parameters needed for the atomistic LLG equation have been evaluated from *ab initio* electronic structure theory. It is worth stressing that we apply the nonlocal damping calculated using a collinear DFT framework ($\boldsymbol{q} = \boldsymbol{0}$) to the noncollinear ($\boldsymbol{q} \neq \boldsymbol{0}$) atomistic spin dynamics (ASD) simulations, which is an approximation in a similar fashion of applying Heisenberg exchange parameters from LKAG (only valid in the long-wavelength limit) to ASD simulations. It would be of great interest to explore the ASD with damping computed using a noncollinear DFT framework [53], but such an investigation is outside the scope of the present work.

Finally, for the calculations shown in Appendix C, we considered special quasirandom structures (SQS) [82]. The SQS cells were created using the MCSQS algorithm within the framework of the Alloy Theoretic Automated Toolkit (ATAT) [83]. We restricted ourselves to the evaluation of a 16-atom SQS cell (or a $2 \times 2 \times 2$ supercell in the perfect bcc lattice, SQS-16), where $Fe_{50}Co_{50}$ contains 8 Fe and 8 Co atoms. The doublet, triplet, and quadruplet correlation distances are set to match, respectively, 3.1, 1.8, and 1.5 lattice constants. In the same Appendix, we also performed calculations by a fully relativistic multiple-scattering Green's function method [Korringa-Kohn-Rostoker method (KKR)] [84], where the LSDA exchange-correlation functional, an irreducible $\boldsymbol{k}$-mesh of $20 \times 20 \times 20$, and the maximal momentum quantum number $l_{\max} = 4$ were adopted in the self-consistent calculations. For the density of states (DOS), we considered a $40 \times 40 \times 40$ $\boldsymbol{k}$-mesh in both CPA and VCA calculations, where the imaginary part of the energy $\delta = 0.005$ Ry was used in the VCA calculations.

III. RESULTS

A. On-site and nonlocal dampings

Table I shows the relevant *ab initio* magnetic properties of each material; the T_C values refer to the Curie temperature calculated within the random-phase approximation (RPA) [85], based on the computed J_{ij} set. Despite the systematic α_{tot} values found in the lower limit of available experimental results

TABLE I. Spin (m_{spin}) and orbital (m_{orb}) magnetic moments, on-site (α_{ii}) damping, total (α_{tot}) damping, and Curie temperature (T_C) of the investigated systems. The theoretical T_C value is calculated within the RPA. In turn, m_t denotes the total moments for experimental results of Ref. [87]. Except for Ref. [32], where the information of temperature is not mentioned, all the other experimental Gilbert damping values are measured at room temperature.

	m_{spin} (μ_B)	m_{orb} (μ_B)	α_{ii} ($\times 10^{-3}$)	α_{tot} ($\times 10^{-3}$)	T_C (K)
bcc Fe (theory)	2.23	0.05	2.4	2.1	919
bcc Fe (expt.)	2.13 [67]	0.08 [67]		1.9–7.2 [32,76,88–93]	1044
bcc $Fe_{70}Co_{30}$ (theory)	2.33	0.07	0.5	0.9	1667
bcc $Fe_{70}Co_{30}$ (expt.)	$m_t = 2.457$ [87]			0.5–1.7[a] [32,88,94]	1258 [96]
bcc $Fe_{50}Co_{50}$ (theory)	2.23	0.08	1.5	1.6	1782
bcc $Fe_{50}Co_{50}$ (expt.)	$m_t = 2.355$ [87]			2.0–3.2[b] [32,88,97]	1242 [98]
fcc Co (theory)	1.62	0.08	7.4	1.4	1273
fcc Co (expt.)	1.68(6) [99]			2.8(5) [32,93]	1392
fcc Ni (theory)	0.61	0.05	160.1	21.6	368
fcc Ni (expt.)	0.57 [67]	0.05 [67]		23.6–64 [22,88,91–93,100,101]	631

[a]The lower limit refers to polycrystalline $Fe_{75}Co_{25}$ 10-nm-thick films from Ref. [32]. Lee *et al.* [94] also found a low Gilbert damping in an analogous system, where $\alpha_{\text{tot}} < 1.4 \times 10^{-3}$. For the exact 30% of Co concentration, however, previous results [32,76,95] indicate that we should expect a slightly higher damping than in $Fe_{75}Co_{25}$.

[b]The upper limit refers to the approximate minimum intrinsic value for a 10-nm-thick film of $Fe_{50}Co_{50}$|Pt (easy magnetization axis).

(in a similar case with, e.g., Ref. [86]), in part explained by the fact that we analyze only the intrinsic damping, a good agreement between theory and experiment can be seen. When the whole VCA $Fe_{1-x}Co_x$ series is considered (from $x = 0\%$ to 60%), the expected Slater-Pauling behavior of the total magnetic moment [72,87] is obtained (data not shown).

For all systems studied here, the dissipation is dominated by the on-site (α_{ii}) term, while the nonlocal parameters (α_{ij}, $i \neq j$) exhibit values at least one order of magnitude lower; however, as will be demonstrated in the next sections, these smaller terms still cause a non-negligible impact on the relaxation of the average magnetization as well as magnon lifetimes. Figure 1 shows the nonlocal damping parameters for the investigated ferromagnets as a function of the (i, j) pairwise distance r_{ij}/a, together with the correspondent Fourier transforms $\alpha_{\boldsymbol{q}}$ over the first Brillouin zone (BZ). The first point to notice is the overall strong dependence of α on the wave vector $\boldsymbol{q}$. The second point is the fact that, as also reported in Ref. [20], α_{ij} can be an anisotropic quantity with respect to the same shell of neighbors, due to the broken symmetry imposed by a preferred spin quantization axis. This means that, in the collinear model and for a given neighboring shell, α_{ij} is isotropic only for equivalent sites around the magnetization as a symmetry axis.

Another important feature that can be seen in Fig. 1 is the presence of negative α_{ij} values. Real-space negative nonlocal damping parameters have been reported previously [20,78,102]. They are related to the decrease of damping at the Γ-point, but they may also increase $\alpha_{\boldsymbol{q}}$ from the on-site value in specific $\boldsymbol{q}$ points inside the BZ; therefore, they cannot be seen as *ad hoc* antidissipative contributions. In the ground state, these negative nonlocal dampings originate from the overlap between the anti-Hermitian parts of the two Green's functions at the Fermi level, each associated with a spin-dependent phase factor Φ^{σ} ($\sigma = \uparrow, \downarrow$) [20,85].

Finally, as shown in the insets of Fig. 1, a long-range convergence can be seen for all cases investigated. An illustrative example is the bcc $Fe_{50}Co_{50}$ bulk, for which the effective damping can be ∼60% higher than the converged α_{tot} if only the first seven shells of neighbors are considered in Eq. (14). The nonlocal damping of each neighboring shell is found to follow a $\frac{1}{r_{ij}^2}$ trend, as previously argued by Thonig *et al.* [20] and Umetsu *et al.* [102]. Explicitly,

$$\alpha_{ij} \propto \frac{\sin(\boldsymbol{k}^{\uparrow} \cdot \boldsymbol{r}_{ij} + \Phi^{\uparrow}) \sin(\boldsymbol{k}^{\downarrow} \cdot \boldsymbol{r}_{ij} + \Phi^{\downarrow})}{|\boldsymbol{r}_{ij}|^2}, \tag{16}$$

which also qualitatively justifies the existence of negative α_{ij}'s. Thus, the convergence in real space is typically slower than other magnetic quantities, such as exchange interactions ($J_{ij} \propto \frac{1}{|\boldsymbol{r}_{ij}|^3}$) [85], and it also depends on the imaginary part δ [see Eq. (15)] [20]. The difference in the asymptotic behavior of the damping and the Heisenberg exchange is distinctive; the first scales with the inverse of the square of the distance, while the latter scales as the inverse of the cube of the distance. Although this asymptotic behavior can be derived from similar arguments, both using the Green's function of the free-electron gas, the results are different. The reason for this difference is simply that the damping parameter is governed by states close to the Fermi surface, while the exchange parameter involves an integral over all occupied states [20,81].

From bcc Fe to bcc $Fe_{50}Co_{50}$ [Figs. 1(a)–1(f)], with increasing Co content, the average first neighbors α_{ij} decrease to a negative value, while the next-nearest-neighbor contributions reach a minimum, and then increase again. Similar oscillations can be found in further shells. Among the interesting features in the $Fe_{1-x}Co_x$ systems ($x = 0\%, 30\%, 50\%$), we highlight the low $\alpha_{\boldsymbol{q}}$ around the high-symmetry point H, along the H-P and H-N directions, consistently lower than the FMR damping. Both α values are strongly influenced by nonlocal contributions $\gtrsim$5 NN. Also consistent is the high $\alpha_{\boldsymbol{q}}$ obtained for $\boldsymbol{q} = \boldsymbol{H}$. For long wavelengths in bcc Fe, some $\alpha_{\boldsymbol{q}}$ anisotropy is observed around Γ, which resembles the same trait obtained for the corresponding magnon dispersion curves [85]. This anisotropy changes to a more isotropic behavior by FeCo alloying.

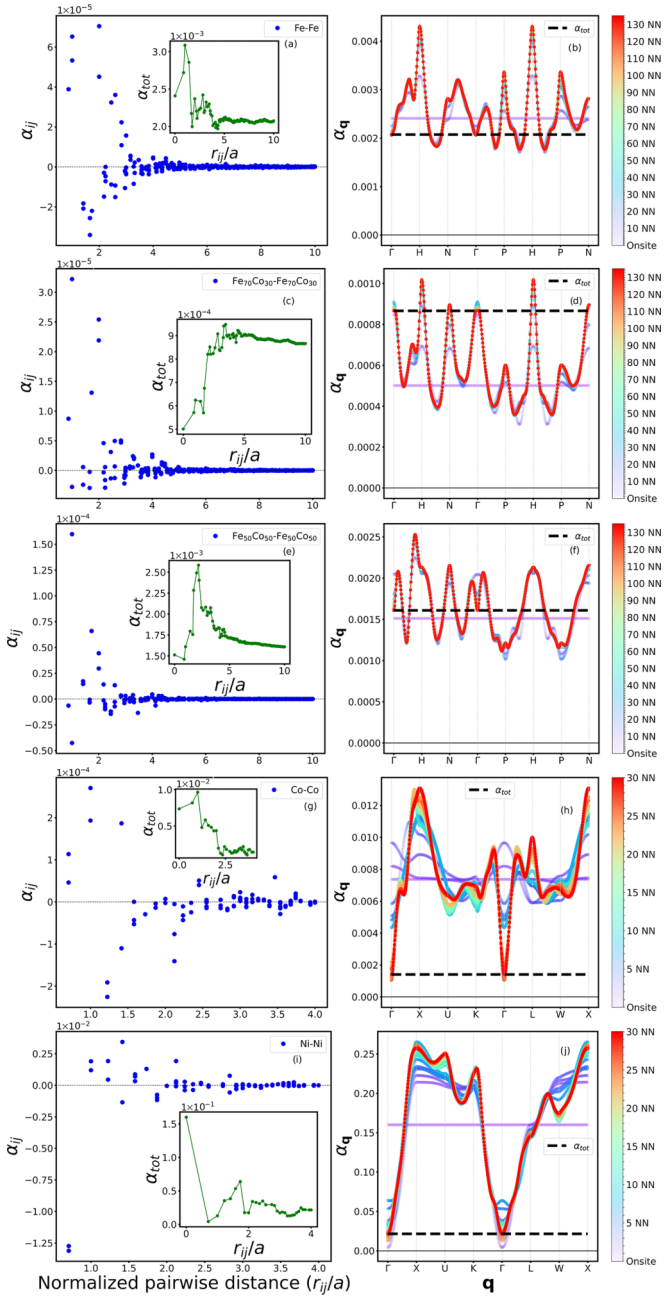

FIG. 1. Nonlocal damping (α_{ij}) as a function of the normalized real-space pairwise (i, j) distance computed for each neighboring shell, and corresponding Fourier transform $\alpha_{\boldsymbol{q}}$ [see Eq. (11)] from the on-site value (α_{ii}) up to 136 shells of neighbors (136 NN) for [(a),(b)] bcc Fe; [(c),(d)] bcc $Fe_{70}Co_{30}$; [(e),(f)] bcc $Fe_{50}Co_{50}$ in the virtual-crystal approximation; and up to 30 shells of neighbors (30 NN) for [(g),(h)] fcc Co; [(i),(j)] fcc Ni. The insets in subfigures (a), (c), (e), (g), and (i) show the convergence of $\alpha_{\rm tot}$ in real space. The obtained on-site damping values are shown in Table I. In the insets of the left panel, green full lines are guides for the eyes. In (b), (d), (f), (h), and (j), the dashed lines correspond to calculations using Eq. (14).

Far from the more noticeable high-symmetry points, $\alpha_{\boldsymbol{q}}$ presents an oscillatory behavior along the BZ, around the on-site value. It is noteworthy, however, that these oscillatory $\alpha_{\boldsymbol{q}}$ parameters exhibit variations up to ∼2 times α_{ii}, thus showing a pronounced nonlocal influence in specific $\boldsymbol{q}$ points.

In turn, for fcc Co [Figs. 1(g) and 1(h)], the first values are characterized by an oscillatory behavior around zero, which also reflects the damping of the FMR mode, $\alpha_{\boldsymbol{q}=\boldsymbol{0}}$. In full agreement with Ref. [20], we compute a peak of α_{ij} contribution at $r_{ij} \sim 3.46a$, which shows the long-range character that nonlocal damping can exhibit for specific materials. Despite the relatively small magnitude of α_{ij}, the multiplicity of the nearest-neighbor shells drives a converged $\alpha_{\boldsymbol{q}}$ dispersion with non-negligible variations from the on-site value along the BZ, especially driven by the negative third neighbors. The maximum damping is found to be in the region around the high-symmetry point X, where the lifetime of magnon excitations are thus expected to be reduced. A similar situation is found for fcc Ni [Figs. 1(i) and 1(j)], where the first neighbors α_{ij} are found to be highly negative, consequently resulting in a spectrum in which $\alpha_{\boldsymbol{q}} > \alpha_{\boldsymbol{q}=\boldsymbol{0}}$ for every $\boldsymbol{q} \neq \boldsymbol{0}$. In contrast with fcc Co, however, no notable peak contributions are found. It is noteworthy that the total damping as well as the local damping of Ni are much higher than in other ferromagnets, which is due to the well-known peak in the minority-spin density of states at E_F in fcc Ni and the scaling factor $\frac{1}{m_t}$ given in Eq. (15).

B. Remagnetization

Gilbert damping in magnetic materials determines the rate of energy that dissipates from the magnetic to other reservoirs, such as phonons or electron excitations. To explore what impact nonlocal damping has on the energy dissipation process, we performed atomistic spin dynamics (ASD) simulations for the aforementioned ferromagnets: Bcc $Fe_{1-x}Co_x$ ($x = 0\%, 30\%, 50\%$), fcc Co, and fcc Ni for the (i) fully nonlocal α_{ij} and (ii) effective $\alpha_{\rm tot}$ [defined in Eq. (14)] dissipative case. We note that, although widely considered in ASD calculations, the adoption of a constant $\alpha_{\rm tot}$ value [case (ii)] is only a good approximation for long-wavelength magnons close to $\boldsymbol{q} = \boldsymbol{0}$.

First, we study the role of nonlocal damping in the remagnetization processes as it was already discussed by Thonig *et al.* [20] and as it is important for, e.g., ultrafast pump-probe experiments as well as all-optical switching, although we note that the model considered here is of limited use in the ultrafast case as the rigid spin approximation breaks down. In the simulations presented here, the relaxation starts from a totally random magnetic configuration. The results of remagnetization simulations are shown in Fig. 2. The fully nonlocal damping (i) in the equation of motion enhances the energy dissipation process compared to the case in which only the effective damping (ii) is used. This effect is found to be more pronounced in fcc Co and fcc Ni compared to bcc Fe and bcc $Fe_{50}Co_{50}$. Thus, the remagnetization time to 90% of the saturation magnetization becomes approximately five to eight times faster for case (i) compared to case (ii). This is due to the increase of $\alpha_{\boldsymbol{q}}$ away from the Γ point in the whole spectrum for Co and Ni (see Fig. 1), where in Fe and $Fe_{50}Co_{50}$ it typically oscillates around $\alpha_{\rm tot}$.

For bcc $Fe_{70}Co_{30}$, the effect of nonlocal damping on the dynamics is opposite to the data in Fig. 2; the relaxation process is decelerated. In this case, almost the entire $\alpha_{\boldsymbol{q}}$ spectrum

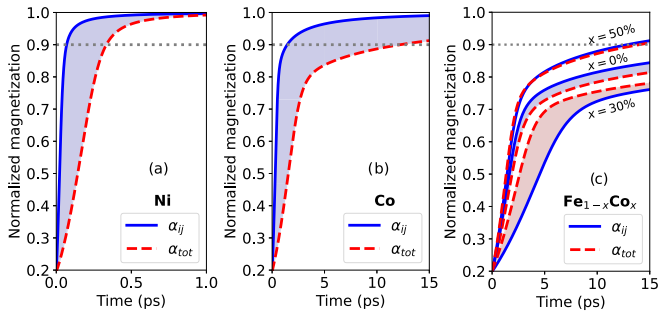

FIG. 2. Remagnetization process simulated with ASD, considering fully nonlocal Gilbert damping (α_{ij}, blue solid lines), and the effective damping (α_{tot}, red dashed lines), for (a) fcc Ni; (b) fcc Co; and (c) bcc $Fe_{1-x}Co_x$ ($x = 0\%, 30\%, 50\%$). The dashed gray lines indicate the stage of 90% of the saturation magnetization.

is below $\alpha_{\boldsymbol{q}=\boldsymbol{0}}$, which is an interesting result given the fact that FMR measurements of the damping parameter in this system are already considered an ultralow value when compared to other metallic ferromagnets [32]. Thus, in the remagnetization process of $Fe_{70}Co_{30}$, the majority of magnon mode lifetimes is underestimated when a constant α_{tot} is considered in the spin dynamics simulations, which leads to a faster overall relaxation rate.

Although bcc Fe presents the highest Gilbert damping obtained in the series of the Fe-Co alloys (see Table I), the remagnetization rate is found to be faster in bcc $Fe_{50}Co_{50}$. This can be explained by the fact that the exchange interactions for this particular alloy are stronger (∼80% higher for nearest neighbors) than in pure bcc Fe, leading to an enhanced Curie temperature (see Table I). In view of Eq. (13) and Fig. 1, the difference in the remagnetization time between bcc $Fe_{50}Co_{50}$ and elemental bcc Fe arises from $\alpha_{\boldsymbol{q}}$ values that are rather close, but where the magnon spectrum of $Fe_{50}Co_{50}$ has much higher frequencies, with corresponding faster dynamics and hence shorter remagnetization times.

From our calculations, we find that the sum of nonlocal damping ($\sum_{i\neq j}\alpha_{ij}$) contributes with −13%, −81%, −87%, +80%, and +7% to the local damping in bcc Fe, fcc Co, fcc Ni, bcc $Fe_{70}Co_{30}$, and bcc $Fe_{50}Co_{50}$, respectively. The high positive ratio found in $Fe_{70}Co_{30}$ indicates that, in contrast to the other systems analyzed, the nonlocal contributions act like an antidamping torque, diminishing the local damping torque. A similar antidamping effect in antiferromagnetic (AFM) materials has been reported in theoretical and experimental investigations (e.g., [103,104]), induced by electrical current. Here we find that an antidamping torque effect can have an intrinsic origin.

To provide a deeper understanding of the antidamping effect caused by a positive nonlocal contribution, we analytically solved the equation of motion for a two-spin model system, e.g., a dimer. In the particular case when the on-site damping α_{11} is equal to the nonlocal contribution α_{12}, we observed that the system becomes undamped (see Appendix B). As demonstrated in Appendix B, ASD simulations of such a dimer corroborate the result of undamped dynamics. Full details of the analytical solution and ASD simulation of a spin-dimer and the antidamping effect are provided in Appendix B.

C. Magnon spectra

To demonstrate the influence of damping on magnon properties at finite temperatures, we have performed ASD simulations to obtain the excitation spectra from the dynamical structure factor introduced in Sec. II. Here, we consider 16 NN shells for $S(\boldsymbol{q}, \omega)$ calculations both from simulations that include nonlocal damping as well as the effective total damping (see Appendix D for a focused discussion). In Fig. 3, the simulated magnon spectra of the ferromagnets investigated here are shown. We note that a general good agreement can be observed between our computed magnon spectra (both from the frozen magnon approach as well as from the dynamical structure factor) and previous theoretical as well as experimental results [33,51,85,105–108], where deviations from experiments are largest for fcc Ni. This exception, however, is well known and has already been discussed elsewhere [109].

The main effect of the nonlocal damping on the magnon spectra in all systems investigated here is that it changes the full width at half-maximum (FWHM) $\triangle_{\boldsymbol{q}}$ of $S(\boldsymbol{q}, \omega)$. Usually, $\triangle_{\boldsymbol{q}}$ is determined from the superposition of thermal fluctuations and damping processes. More specifically, the nonlocal damping broadens the FWHM compared to simulations based solely on an effective damping for most of the high-symmetry paths in all of the ferromagnets analyzed here, with the exception of $Fe_{70}Co_{30}$. The most extreme case is for fcc Ni, as $\alpha_{\boldsymbol{q}}$ exceeds the 0.25 threshold for $\boldsymbol{q} = \boldsymbol{X}$, which is comparable to the damping of ultrathin magnetic films on high-SOC metallic hosts [110]. As a comparison, the largest difference of FWHM between the nonlocal damping process and the effective damping process in bcc Fe is ∼2 meV, while in fcc Ni the largest difference can reach ∼258 meV. In contrast, the difference is ∼ − 1 meV in $Fe_{70}Co_{30}$, and the largest nonlocal damping effect occurs around $\boldsymbol{q} = \boldsymbol{N}$ and in the H-P direction, corroborating the discussion in Sec. III A. At the Γ point, which corresponds to the mode measured in FMR experiments, all spins in the system have a coherent precession. This implies that $\frac{\partial \boldsymbol{m}_i}{\partial t}$ in Eq. (4) is the same for all moments, and thus both damping scenarios discussed here (the effective damping and fully nonlocal damping) make no difference to the spin dynamics. As a consequence, only a tiny (negligible) difference of the FWHM is found between effective and nonlocal damping for the FMR mode at low temperatures.

The broadening of the FWHM on the magnon spectrum is temperature-dependent. Thus, the effect of nonlocal damping to the width near Γ can be of great interest for experiments. More specifically, taking bcc Fe as an example, the difference between the width in the effective damping and the nonlocal damping processes increases with temperature, where the difference can be enhanced up to one order of magnitude from $T = 0.1$ to 25 K. Note that this enhancement might be misleading due to the limits of the finite-temperature assumption made here. This temperature-dependent damping effect on FWHM suggests a path for the measurement of nonlocal damping in FMR experiments.

We have also compared the difference in the imaginary part of the transverse dynamical magnetic susceptibility computed from nonlocal and effective damping. Defined by Eq. (12), the imaginary part of the susceptibility is related to the FWHM

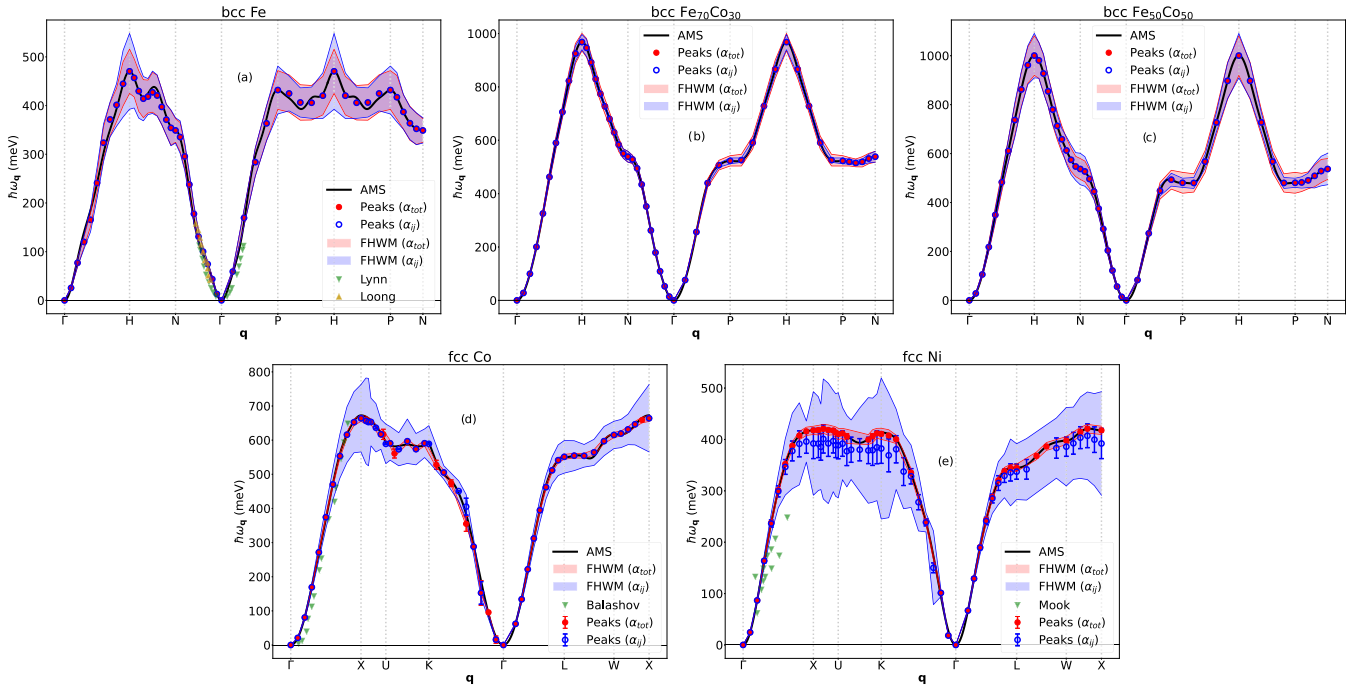

FIG. 3. Magnon spectra calculated with nonlocal Gilbert damping and effective Gilbert damping in (a) bcc Fe; (b) bcc $Fe_{70}Co_{30}$; (c) bcc $Fe_{50}Co_{50}$; (d) fcc Co; and (e) fcc Ni. The black lines denote the adiabatic magnon spectra calculated from Eq. (7). Full red and open blue points denote the peak positions of $S(\boldsymbol{q}, \omega)$ at each $\boldsymbol{q}$ vector for α_{tot} and α_{ij} calculations, respectively, at $T = 0.1$ K. The width of transparent red and blue areas corresponds to the full width at half-maximum (FWHM) on the energy axis fitted from a Lorentzian curve, following the same color scheme. To highlight the difference of the FWHM between the two damping modes, the FWHMs shown in the magnon spectrum of $Fe_{1-x}Co_x$, Co, and Ni are multiplied by 20, 5, and $\frac{1}{2}$ times, in that order. The triangles represent experimental results in (a) Fe at 10 K [107] (yellow up) and Fe with 12% Si at room temperature [106] (green down); in (d) Co(9 ML)/Cu(100) at room temperature [108] (green down); and in (e) Ni at room temperature (green down) [105]. The standard deviation of the peaks is represented as error bars.

[15]. Similar to the magnon spectra shown in Fig. 3, the susceptibility difference is significant at the BZ boundaries. Taking the example of fcc Co, $\text{Im}\chi^{\pm}(\mathbf{q}, \omega)$ for effective damping processes can be 11.8 times larger than in simulations that include nonlocal damping processes, which is consistent with the lifetime peak that occurs at the high-symmetry point, X, depicted in Fig. 4. In the $Fe_{1-x}Co_x$ alloy and $Fe_{70}Co_{30}$, the largest ratio is 1.7 and 2.7, respectively. The intensity at Γ point is zero since $\alpha_{\mathbf{q}}$ is independent of the coupling vector and equivalent in both damping modes. The effect of nonlocal damping on susceptibility coincides well with the magnon spectra from spin dynamics. Thus, this method allows us to evaluate the magnon properties in a more efficient way.

D. Magnon lifetimes

By fitting the $S(\boldsymbol{q}, \omega)$ curve at each wave vector with a Lorentzian curve, the FWHM and hence the magnon lifetimes, $\tau_{\boldsymbol{q}}$, can be obtained from the simple relation [15]

$$\tau_{\boldsymbol{q}} = \frac{2\pi}{\triangle_{\boldsymbol{q}}}. \tag{17}$$

Figure 4 shows the lifetimes computed in the high-symmetry lines in the BZ for all ferromagnets investigated herein. As expected, $\tau_{\boldsymbol{q}}$ is much lower at the $\mathbf{q}$ vectors far away from the zone center, being of the order of 1 ps for the $Fe_{1-x}Co_x$ alloys ($x = 0\%, 30\%, 50\%$), and from $\sim$0.01 to 1 ps in fcc Co and Ni. In view of Eq. (13), the magnon lifetime is inversely proportional to both damping and magnon frequency. In the effective damping process, $\alpha_{\mathbf{q}}$ is a constant and independent of $\boldsymbol{q}$; thus, the lifetime in the entire BZ is dictated only by $\omega_{\boldsymbol{q}}$. The situation becomes more complex in the nonlocal damping process, where the $\tau_{\boldsymbol{q}}$ is influenced by the combined effect of changing damping and magnon frequency. Taking $Fe_{70}Co_{30}$ as an example, even though the $\alpha_{\boldsymbol{q}}$ is higher around the Γ, the low magnon frequency compensates for the damping effect, leading to an asymptotically divergent magnon lifetime as $\omega_{\boldsymbol{q}} \to 0$. However, this divergence becomes finite when including, e.g., magnetocrystalline anisotropy or an external magnetic field to the spin-Hamiltonian. In the H-N path, the magnon energy of $Fe_{70}Co_{30}$ is large, but $\alpha_{\boldsymbol{q}}$ reaches $\sim 4 \times 10^{-4}$ at $\boldsymbol{q} = (\frac{1}{4}, \frac{1}{4}, \frac{1}{2})$, resulting in a magnon lifetime peak of $\sim$10 ps. This value is not found for the effective damping model.

In the elemental ferromagnets, as well as for $Fe_{50}Co_{50}$, it is found that nonlocal damping decreases the magnon lifetimes. This nonlocal damping effect is significant in both Co and Ni, where the magnon lifetimes from the α_{ij} model differ by an order of magnitude from the effective model (see Fig. 4). In fact, considering $\tau_{\boldsymbol{q}}$ obtained from Eq. (13), the effective model predicts a lifetime already higher by more than 50% when the magnon frequencies are $\sim$33 and $\sim$14 meV in the K-Γ path (i.e., near Γ) of Ni and Co, respectively. This difference mainly arises, in real space, from the strong negative contributions of α_{ij} in the close neighborhood around the

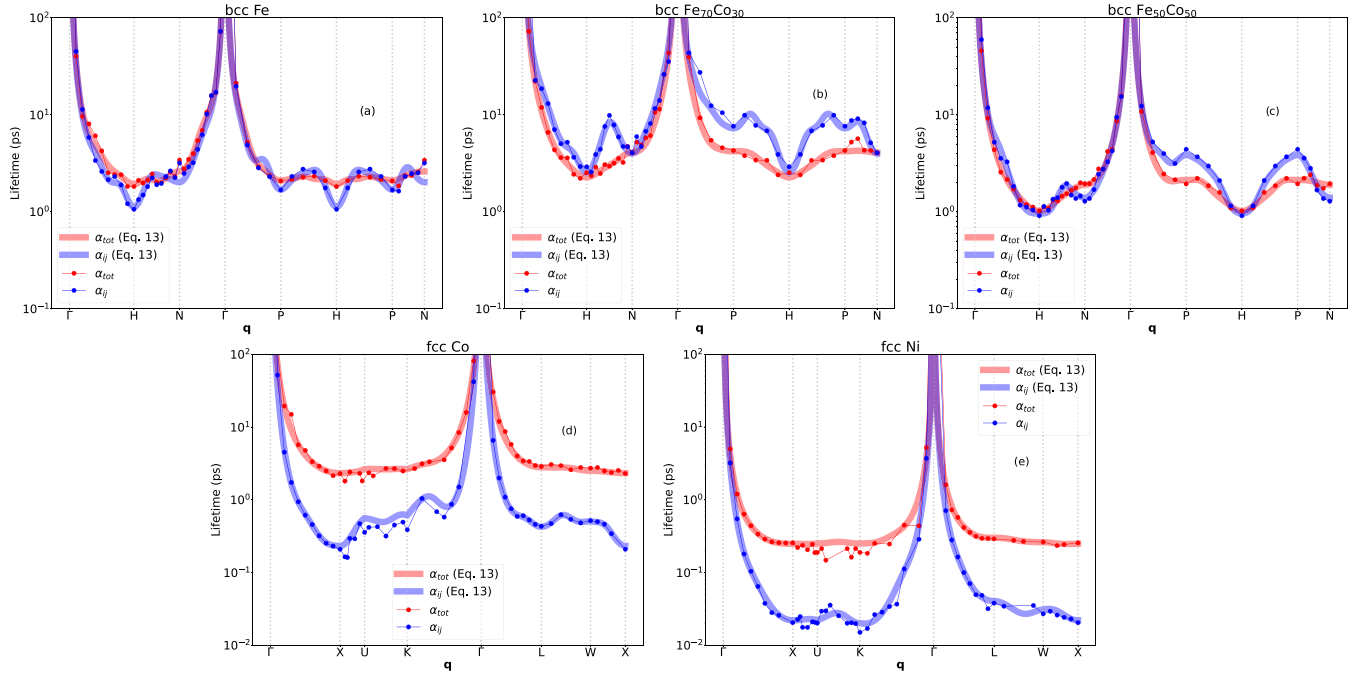

FIG. 4. Magnon lifetimes $\tau_{\boldsymbol{q}}$ of (a) bcc Fe; (b) bcc $Fe_{70}Co_{30}$; (c) bcc $Fe_{50}Co_{50}$; (d) fcc Co; and (e) fcc Ni as a function of $\boldsymbol{q}$, shown in logarithmic scale. The color scheme is the same as Fig. 3, where blue and red represents $\tau_{\boldsymbol{q}}$ computed in the effective and nonlocal damping models. The transparent lines and points depict the lifetimes calculated with Eq. (13) and by the FWHM of $S(\boldsymbol{q}, \omega)$ at $T = 0.1$ K [see Eq. (17)], respectively. The lifetime asymptotically diverges around the Γ-point due to the absence of anisotropy effects or external magnetic field in the spin-Hamiltonian.

reference site, namely the NN in Ni and third neighbors in Co. In contrast, due to the $\alpha_{\boldsymbol{q}}$ spectrum composed of almost all dampings lower than α_{tot}, already discussed in Sec. III A, the opposite trend on $\tau_{\boldsymbol{q}}$ is observed for $Fe_{70}Co_{30}$: The positive overall nonlocal damping contribution results in an antidamping effect, and the lifetimes are enhanced in the nonlocal model.

Another way to evaluate the magnon lifetimes is from the linear-response theory. As introduced in Sec. II B, we have access to magnon lifetimes at low temperatures from the imaginary part of the susceptibility. The $\tau_{\boldsymbol{q}}$ calculated from Eq. (13) is also displayed in Fig. 4. Here the spin-wave frequency $\omega_{\boldsymbol{q}}$ is from the frozen magnon method. The magnon lifetimes from linear response are in very good agreement with the results from the dynamical structure factor, showing the equivalence between both methods. Some of the small discrepancies are related to magnon-magnon scattering induced by the temperature effect in the dynamical structure factor method. We also find good agreement on the magnon lifetimes of effective damping in pure Fe with previous studies [111]. They are in a similar order and decrease with increasing magnon energy. However, their results are more diffused since the simulations are performed at room temperature.

IV. CONCLUSION

We have presented the influence of nonlocal damping on spin dynamics and magnon properties of elemental ferromagnets (bcc Fe, fcc Co, fcc Ni) and the bcc $Fe_{70}Co_{30}$ and bcc $Fe_{50}Co_{50}$ alloys in the virtual-crystal approximation. It is found that the nonlocal damping has important effects on relaxation processes and magnon properties. Regarding the relaxation process, the nonlocal damping in Fe, Co, and Ni has a negative contribution to the local (on-site) part, which accelerates the remagnetization. Contrarily, influenced by the positive contribution of α_{ij} $(i \neq j)$, the magnon lifetimes of $Fe_{70}Co_{30}$ and $Fe_{50}Co_{50}$ are increased in the nonlocal model, typically at the boundaries of the BZ, decelerating the remagnetization.

Concerning the magnon properties, the nonlocal damping has a significant effect in Co and Ni. More specifically, the magnon lifetimes can be overestimated by an order of magnitude in the effective model for these two materials. In real space, this difference arises as a result of strong negative nonlocal contributions in the close neighborhood around the reference atom, namely the NN in Ni and the third neighbors in Co.

Although the effect of nonlocal damping to the stochastic thermal field in spin dynamics is not included in this work, we still obtain coherent magnon lifetimes compared to the analytical solution from linear-response theory. Notably, it is predicted that the magnon lifetimes at certain wave vectors are higher for the nonlocal damping model in some materials. An example is $Fe_{70}Co_{30}$, in which the lifetime can be $\sim$3 times higher in the H-N path for the nonlocal model. On the other hand, we have proposed a fast method based on linear response to evaluate these lifetimes, which can be used in high-throughput computations of magnonic materials. However, the applied VCA theory on an alloy has discarded the short-range disorder in alloys. Hence, the local environmental effects on their damping and magnon properties need further investigation.

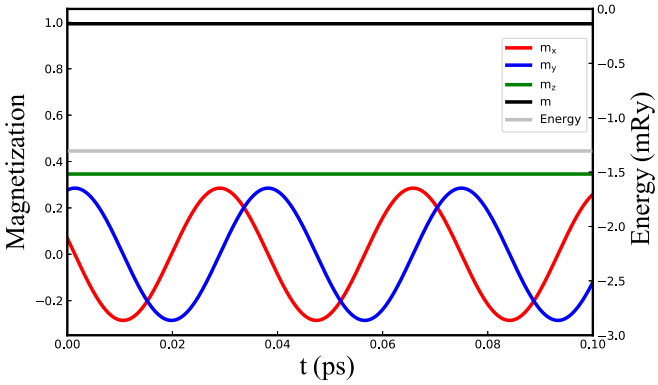

FIG. 5. Spin dynamics at $T = 0$ K of an undamped dimer in which $\alpha_{12} = \alpha_{21} = \alpha_{11}$ (see text). The vector $\boldsymbol{m}_1$ is normalized and its Cartesian components are labeled in the figure as m_x, m_y, and m_z. The black and gray lines indicate the length of spin and energy (in mRy), respectively.

Finally, our study provides a link on how nonlocal damping can be measured in FMR and neutron scattering experiments. Even further, it gives insight into optimizing excitation of magnon modes with possible long lifetimes. This optimization is important for any spintronics applications. As a natural consequence of any real-space *ab initio* formalism, our methodology and findings also open routes for the investigation of other materials with preferably longer lifetimes caused by nonlocal energy dissipation at low excitation modes. Such materials research could also include tuning the local chemical environments by doping or defects.

ACKNOWLEDGMENTS

Financial support from Vetenskapsrådet (Grants No. VR 2016-05980, No. VR 2019-05304, and No. VR 2019-03666), the Knut and Alice Wallenberg foundation (Grant No. 2018.0060), the Foundation for Strategic Research (SSF), the Swedish Energy Agency (Energimyndigheten), the European Research Council (854843-FASTCORR), the China Scholarship Council (CSC), eSSENCE, and STandUP is acknowledged. The computations/data handling were enabled by resources provided by the Swedish National Infrastructure for Computing (SNIC) at the National Supercomputing Centre (NSC, Tetralith cluster), partially funded by the Swedish Research Council through Grant Agreement No. 2016-07213.

APPENDIX A: NUMERICAL SOLVER

In this Appendix, the numerical method to solve Eq. (1) is described. In previous studies, several numerical approaches have been proposed to solve the local LLG equations, including the HeunP method, the implicit midpoint method, Depondt-Merten's method [112], and the semi-implicit A (SIA) and semi-implicit B (SIB) methods [41]. To solve this nonlocal LLG equation, we use the fixed-point iteration midpoint method. We have done convergence tests on this method and find that it preserve the energy and spin length of the system, which is demonstrated in Fig. 5 for the case of a dimer. With stable outputs, the solver allows for a relatively large time step size, typically of the order of $\Delta t \sim 0.1$–1 fs.

Following the philosophy of an implicit midpoint method, the implemented algorithm can be described as follows. Let $\boldsymbol{m}_i^t$ be the magnetic moment of site i at a given time step t. Then we can define the quantity $\boldsymbol{m}_{\text{mid}}$ and the time derivative of $\boldsymbol{m}_i$, respectively, as

$$\begin{aligned} \boldsymbol{m}_{\text{mid}} &= \frac{\boldsymbol{m}_i^{t+1} + \boldsymbol{m}_i^t}{2}, \\ \frac{\partial \boldsymbol{m}_i}{\partial t} &= \frac{\boldsymbol{m}_i^{t+1} - \boldsymbol{m}_i^t}{\Delta t}. \end{aligned} \tag{A1}$$

Using this definition in Eq. (4), the equation of motion of the ith spin becomes

$$\frac{\partial \boldsymbol{m}_i}{\partial t} = \boldsymbol{m}_{\text{mid}} \times \left(-\gamma [\boldsymbol{B}_i(\boldsymbol{m}_{\text{mid}}) + \boldsymbol{b}_i(t)] + \sum_j \frac{\alpha_{ij}}{m_j} \frac{\partial \boldsymbol{m}_j}{\partial t} \right). \tag{A2}$$

Thus, with a fixed-point scheme, we can do the following iteration:

$$\boldsymbol{m}_i^{t+1(k+1)} = \boldsymbol{m}_i^t + \Delta t \left\{ \left(\frac{\boldsymbol{m}_i^{t+1(k)} + \boldsymbol{m}_i^t}{2} \right) \times \left(-\gamma \left[\boldsymbol{B}_i \left(\frac{\boldsymbol{m}_i^{t+1(k)} + \boldsymbol{m}_i^t}{2} \right) + \boldsymbol{b}_i(t) \right] + \sum_j \frac{\alpha_{ij}}{m_j} \frac{\boldsymbol{m}_j^{t+1(k)} - \boldsymbol{m}_j^t}{\Delta t} \right) \right\}. \tag{A3}$$

If $\boldsymbol{m}_i^{t+1(k+1)} \approx \boldsymbol{m}_i^{t+1(k)}$, the self-consistency converges. Typically, about six iteration steps are needed. This solver was implemented in the software package UPPASD [47] for this work.

APPENDIX B: ANALYTICAL MODEL OF ANTIDAMPING IN DIMERS

In the dimer model, there are two spins on site 1 and site 2 denoted by $\boldsymbol{m}_1$ and $\boldsymbol{m}_2$, which are supposed to be related here to the same element—so that, naturally, $\alpha_{11} = \alpha_{22} > 0$. Also, let us consider a sufficiently low temperature so that $\boldsymbol{b}_i(t) \to \boldsymbol{0}$, which is a reasonable assumption, given that damping has an intrinsic origin [113]. This simple system allows us to provide explicit expressions for the Hamiltonian, the effective magnetic fields, and the damping term. From the analytical solution, it is found that the dimer spin system becomes an undamped system when local damping is equal to nonlocal damping, i.e., the effective damping of the system is zero.

Following the definition given by Eq. (4) in the main text, the equation of motion for spin 1 reads

$$\frac{\partial \boldsymbol{m}_1}{\partial t} = \boldsymbol{m}_1 \times \left(-\gamma \boldsymbol{B}_1 + \frac{\alpha_{11}}{m_1} \frac{\partial \boldsymbol{m}_1}{\partial t} + \frac{\alpha_{12}}{m_2} \frac{\partial \boldsymbol{m}_2}{\partial t} \right), \tag{B1}$$

and an analogous expression can be written for spin 2. For the sake of simplicity, the Zeeman term is zero and the effective field only includes the contribution from Heisenberg exchange interactions. Thus, we have $\boldsymbol{B}_1 = 2J_{12}\boldsymbol{m}_2$ and $\boldsymbol{B}_2 = 2J_{21}\boldsymbol{m}_1$. With $|\alpha_{ij}| \ll 1$, we can take the LL form $\frac{\partial \boldsymbol{m}_i}{\partial t} = -\gamma \boldsymbol{m}_i \times \boldsymbol{B}_i$ to approximate the time derivative on the right-hand side of the LLG equation. Let $m_1 = m_2$ and $\alpha_{12} = \lambda\alpha_{11}$. Since $J_{12} = J_{21}$ and $\boldsymbol{m}_1 \times \boldsymbol{m}_2 = -\boldsymbol{m}_2 \times \boldsymbol{m}_1$, we then have

$$\frac{\partial \boldsymbol{m}_1}{\partial t} = -2\gamma J_{12}\boldsymbol{m}_1 \times \left[\boldsymbol{m}_2 + (1-\lambda)\frac{\alpha_{11}}{m_1}(\boldsymbol{m}_1 \times \boldsymbol{m}_2)\right]. \quad \text{(B2)}$$

Therefore, when $\alpha_{12} = \alpha_{21} = \alpha_{11}$ (i.e., $\lambda = 1$), Eq. (B1) is reduced to

$$\frac{\partial \boldsymbol{m}_1}{\partial t} = -2\gamma J_{12}\boldsymbol{m}_1 \times \boldsymbol{m}_2, \quad \text{(B3)}$$

and the system becomes undamped. It is, however, straightforward that, for the opposite case of a strong negative nonlocal damping ($\lambda = -1$), Eq. (B2) describes a common damped dynamics. A side (and related) consequence of Eq. (B2), but important for the discussion in Sec. III B, is the fact that the effective on-site damping term $\alpha_{11}^* = (1-\lambda)\alpha_{11}$ becomes less relevant to the dynamics as the positive nonlocal damping increases ($\lambda \to 1$), or, in other words, as $\alpha_{\text{tot}} = (\alpha_{11} + \alpha_{12})$ strictly increases due to the nonlocal contribution. Exactly the same reasoning can be made for a trimer, for instance, composed by atoms with equal moments and exchange interactions ($m_1 = m_2 = m_3$, $J_{12} = J_{13} = J_{23}$), and the same nonlocal dampings ($\alpha_{13} = \alpha_{12} = \lambda\alpha_{11}$).

The undamped behavior can be directly observed from ASD simulations of a dimer with $\alpha_{12} = \alpha_{11}$, as shown in Fig. 5. Here the magnetic moment and the exchange are taken the same as those of an Fe dimer, $m_1 = 2.23\mu_B$ and $J_{12} = 1.34$ mRy. Nevertheless, obviously the overall behavior depicted in Fig. 5 is not dependent on the choice of $\boldsymbol{m}_1$ and J_{12}. The z component is constant, while the x and y components of $\boldsymbol{m}_1$ oscillate in time, indicating a precessing movement.

In a broader picture, this simple dimer case exemplifies the connection between the eigenvalues of the damping matrix $\boldsymbol{\alpha} = (\alpha_{ij})$ and the damping behavior. The occurrence of such undamped dynamics has been recently discussed in Ref. [114], where it is shown that a dissipation-free mode can occur in a system composed of two subsystems coupled to the same bath.

APPENDIX C: EFFECTIVE AND ON-SITE DAMPING IN THE FECO AND CONI ALLOYS

As mentioned in Sec. II, the simple VCA model allows us to account for the disorder in 3d-transition-metal alloys in a crude but efficient way that avoids the use of large supercells with random chemical distributions. With exactly the same purpose, the CPA [115] has also been employed to analyze damping in alloys (e.g., in Refs. [76,77,116]), showing a very good output with respect to trends, when compared to experiments [32,86]. In Fig. 7 we show the normalized calculated local (on-site, α_{ii}) and effective damping (α_{tot}) parameters for the zero-temperature VCA $Fe_{1-x}Co_x$ alloy in the bcc structure, consistent with a concentration up to $x \approx 60\%$ of Co [32]. The computed values in this work (blue points representing α_{ii}, and red points representing α_{tot}) are compared to previous theoretical CPA results and room-temperature experimental data. The trends with VCA are reproduced in good agreement with respect to experiments and CPA calculations, showing a minimal α_{tot} when the Co concentration is $x \approx 30\%$. This behavior is well correlated with the local density of states (LDOS) at the Fermi level, as expected by the simplified Kamberský equation [117], and the on-site contribution. Although the scattering of electrons could be distinct for Fe and Co due to the differences in the (narrow) d bands [118], these local environment effects are less pronounced when comparing the total density of states coming from VCA and CPA approaches, and even from an explicit SQS cell (average DOS/atom) for the $Fe_{50}Co_{50}$ alloy—especially near (and at) the Fermi level. Figure 6 shows the total DOSs comparison between (a) VCA and

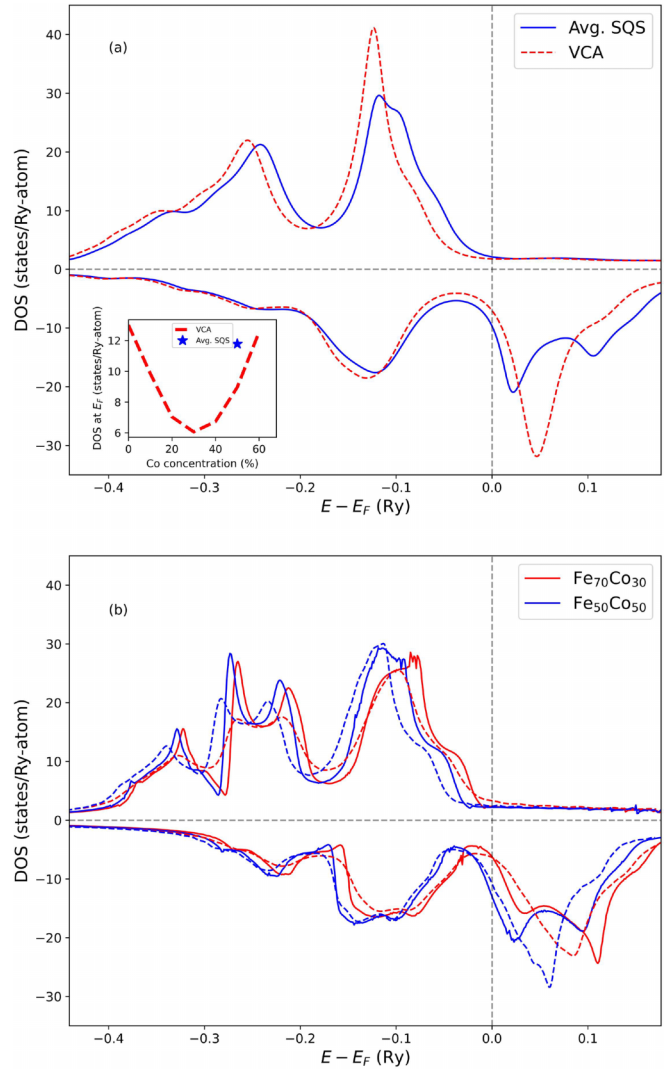

FIG. 6. Comparisons between the total density of states calculated from (a) $Fe_{50}Co_{50}$ SQS-16 cell (blue solid lines) and $Fe_{50}Co_{50}$ VCA (red dashed lines); and (b) CPA (solid lines) and VCA (dashed lines) via the KKR approach for bcc $Fe_{1-x}Co_x$ alloys: $Fe_{70}Co_{30}$ (in red) and $Fe_{50}Co_{50}$ (in blue). In the inset of (a) we show the relation between the total DOS at E_F calculated with VCA and the SQS-16 cell.

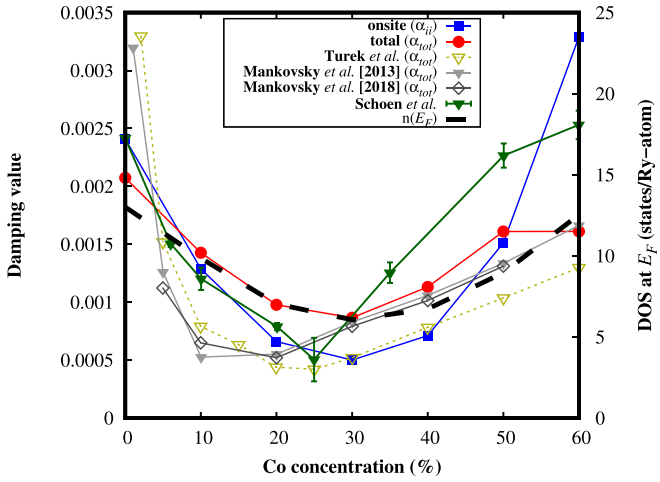

FIG. 7. Left scale: Computed Gilbert effective (α_{tot}, red circles) and on-site (α_{ii}, blue squares) damping parameters as a function of Co the concentration (x) for bcc $Fe_{1-x}Co_x$ binary alloy in the virtual-crystal approximation. The values are compared with previous theoretical results using CPA at 0 K, from Ref. [76] (gray full triangles), Ref. [53] (black open rhombus), Ref. [77] (yellow open triangles), and room-temperature experimental data [32] (green full triangles). Right scale: The calculated density of states (DOS) at the Fermi level as a function of x, represented by the black dashed line.

the SQS-16 cell, both calculated with the RS-LMTO-ASA method, and (b) VCA and CPA, obtained with the KKR method [84]. Despite the good agreement found, the values we have determined are subjected to a known error of the VCA with respect to the experimental results.

This discrepancy can be partially explained by three reasons: (i) the significant influence of local environments (local

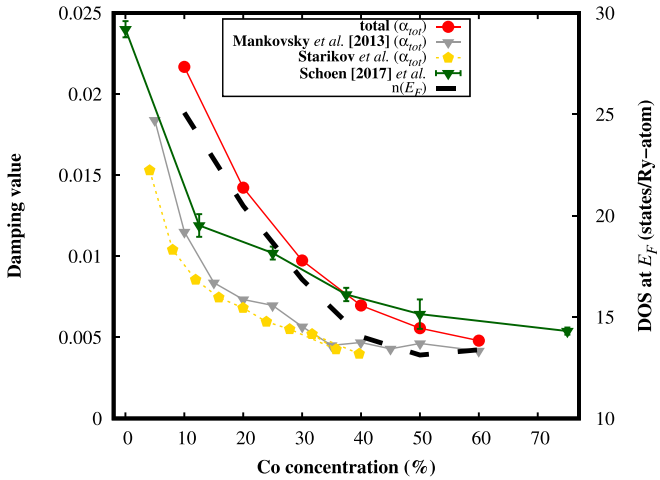

FIG. 8. Left scale: Computed Gilbert effective (α_{tot}, red circles) damping parameters as a function of the Co concentration (x) for fcc Co_xNi_{1-x} binary alloy in the virtual-crystal approximation. The values are compared with previous theoretical results using CPA at 0 K from Ref. [76] (gray full triangles), Ref. [86] (gold full circles), and room-temperature experimental data [93] (green full triangles). Right scale: The calculated density of states (DOS) at the Fermi level as a function of x, represented by the black dashed line.

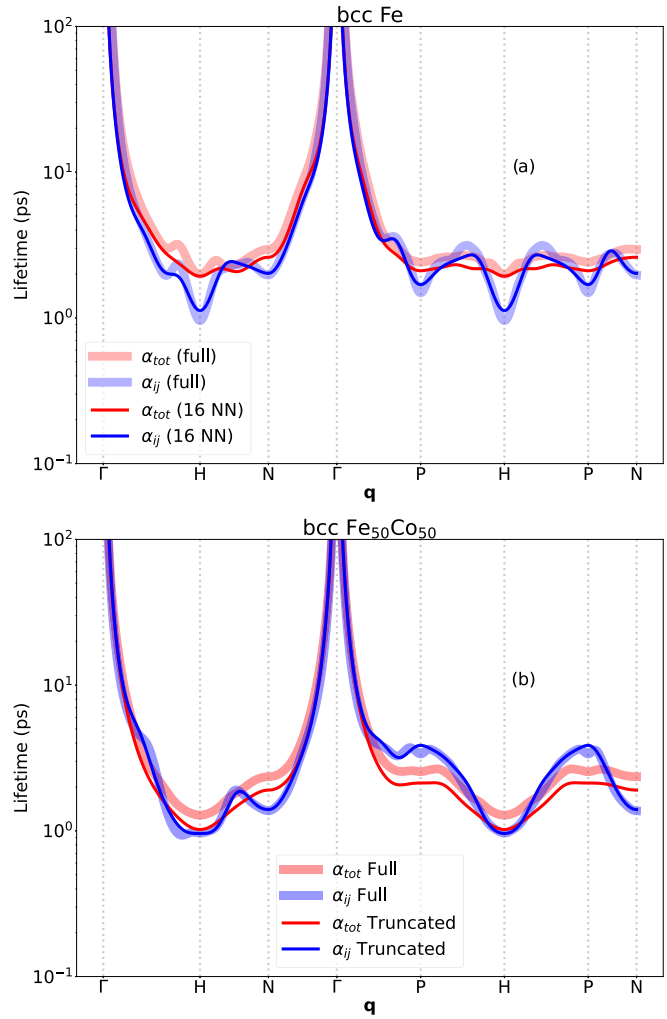

FIG. 9. Magnon lifetimes calculated using Eq. (13) for (a) bcc Fe and (b) bcc $Fe_{50}Co_{50}$, using a reduced set of 16 NN shells (opaque lines), and the full set of 136 NN shells (transparent lines).

disorder and/or short-range order) to α_{tot} [78,97]; (ii) the fact that the actual electronic lifetime (i.e., the mean time between two consecutive scattering events) is subestimated by the VCA average for randomness in the FeCo alloy, which can have a non-negligible impact on the damping parameter [22,119]; and (iii) the influence on damping of noncollinear spin configurations in finite-temperature measurements [53,120]. On top of that, it is noticeable that the damping is dependent on the broadening of electron energy states [22,119], δ, that is associated with numerous electron lifetime-limiting effects, e.g., electron-phonon coupling and thermal vibrations, defect concentration, and electron-electron interaction beyond DFT. Given the multifaceted nature of this broadening, δ is sometimes used as an empirical quantity to bring theory into agreement with experiments. In this work, the imaginary part of the energy is not an explicit parameter, which is related to the number of recursion levels LL. The convergence test on damping has been performed to ensure the LL value is sufficient (not shown).

In the spirit of demonstrating the effectiveness of the simple VCA to qualitatively (and also, to some extent,

quantitatively) describe the properties of Gilbert damping (see Fig. 7) in suitable magnetic alloys, we also show in Fig. 8 the results obtained for Co_xNi_{1-x} systems. The CoNi alloys are known to form in the fcc structure for a Ni concentration range of 10–100 %. Therefore, here we modeled Co_xNi_{1-x} by a big fcc cluster containing ∼530 000 atoms in real-space with the equilibrium lattice parameter of $a = 3.46$ Å. The number of recursion levels considered is $LL = 41$. A good agreement with experimental results and previous theoretical calculations can be noticed. In particular, the qualitative comparison with theory from Refs. [76,86] indicates the equivalence between the torque correlation and the spin correlation models for calculating the damping parameter, which was also investigated by Sakuma [121]. The on-site contribution for each Co concentration, α_{ii}, is omitted from Fig. 8 due to an absolute value two to four times higher than α_{tot}, but it follows the same decreasing trend. Again, the overall effective damping values are well correlated with the LDOS, and they reflect the variation of the quantity $\frac{1}{m_t}$ with Co concentration [see Eq. (15)].

APPENDIX D: EFFECT OF FURTHER NEIGHBORS IN THE MAGNON LIFETIMES

When larger cutoff radii (R_{cut}) of α_{ij} parameters are included in ASD, Eq. (A3) takes longer times to achieve a self-consistent convergence. In practical terms, to reach a sizable computational time for the calculation of a given system, R_{cut} needs to be chosen in order to preserve the main features of the magnon properties as if $R_{\text{cut}} \to \infty$. A good quantity to rely on is the magnon lifetime $\tau_{\mathbf{q}}$, as it consists of both magnon frequency and $\mathbf{q}$-resolved damping [Eq. (13)]. In Sec. III C, we have shown the equivalence between Eq. (13) and the inverse of the FWHM on the energy axis of $S(\mathbf{q}, \omega)$ for the ferromagnets investigated here. Thus, the comparison of two $\tau_{\mathbf{q}}$ spectra for different R_{cut} can be done directly and in an easier way using Eq. (13).

An example is shown in Fig. 9 for bcc Fe and bcc $Fe_{50}Co_{50}$. Here we choose the first 16 NN ($R_{\text{cut}} \sim 3.32a$) and compare the results with the fully calculated set of 136 NN ($R_{\text{cut}} = 10a$). It is noticeable that the reduced set of neighbors can capture most of the features of the $\tau_{\mathbf{q}}$ spectrum for a full NN set. However, long-range influences of small magnitudes, such as extra oscillations around the point $\mathbf{q} = \mathbf{H}$ in Fe, can occur. In particular, these extra oscillations arise mainly due to the presence of Kohn anomalies in the magnon spectrum of Fe, already reported in previous works [51,85]. In turn, for the case of $Fe_{50}Co_{50}$, the long-range α_{ij} reduces α_{tot}, and causes the remagnetization times for nonlocal and effective dampings to be very similar (see Fig. 2). For the other ferromagnets considered in the present research, comparisons of the reduced R_{cut} with analogous quality were reached.

[1] A. Barman, G. Gubbiotti, S. Ladak, A. O. Adeyeye, M. Krawczyk, J. Gräfe, C. Adelmann, S. Cotofana, A. Naeemi, V. I. Vasyuchka *et al.*, J. Phys.: Condens. Matter **33**, 413001 (2021).

[2] P. Pirro, V. I. Vasyuchka, A. A. Serga, and B. Hillebrands, Nat. Rev. Mater. **6**, 1114 (2021).

[3] B. Rana and Y. Otani, Commun. Phys. **2**, 90 (2019).

[4] A. Mahmoud, F. Ciubotaru, F. Vanderveken, A. V. Chumak, S. Hamdioui, C. Adelmann, and S. Cotofana, J. Appl. Phys. **128**, 161101 (2020).

[5] A. Serga, A. Chumak, and B. Hillebrands, J. Phys. D **43**, 264002 (2010).

[6] S. Lendinez and M. Jungfleisch, J. Phys.: Condens. Matter **32**, 013001 (2020).

[7] K. Zakeri, J. Phys.: Condens. Matter **32**, 363001 (2020).

[8] D. D. Awschalom, C. Du, R. He, J. Heremans, A. Hoffmann, J. Hou, H. Kurebayashi, Y. Li, L. Liu, V. Novosad *et al.*, IEEE Trans. Quantum Eng. **2**, 1 (2021).

[9] Z. Chen and F. Ma, J. Appl. Phys. **130**, 090901 (2021).

[10] B. Lenk, H. Ulrichs, F. Garbs, and M. Münzenberg, Phys. Rep. **507**, 107 (2011).

[11] C. Liu, J. Chen, T. Liu, F. Heimbach, H. Yu, Y. Xiao, J. Hu, M. Liu, H. Chang, T. Stueckler *et al.*, Nat. Commun. **9**, 738 (2018).

[12] L. Sheng, J. Chen, H. Wang, and H. Yu, J. Phys. Soc. Jpn. **90**, 081005 (2021).

[13] C. Burrowes, B. Heinrich, B. Kardasz, E. Montoya, E. Girt, Y. Sun, Y.-Y. Song, and M. Wu, Appl. Phys. Lett. **100**, 092403 (2012).

[14] M. Correa, J. Santos, B. Silva, S. Raza, R. Della Pace, C. Chesman, R. Sommer, and F. Bohn, J. Magn. Magn. Mater. **485**, 75 (2019).

[15] O. Eriksson, A. Bergman, L. Bergqvist, and J. Hellsvik, *Atomistic Spin Dynamics: Foundations and Applications* (Oxford University Press, Oxford, 2017).

[16] T. L. Gilbert, IEEE Trans. Magn. **40**, 3443 (2004).

[17] K. Gilmore, M. D. Stiles, J. Seib, D. Steiauf, and M. Fähnle, Phys. Rev. B **81**, 174414 (2010).

[18] M. Fähnle and D. Steiauf, Phys. Rev. B **73**, 184427 (2006).

[19] S. Bhattacharjee, L. Nordström, and J. Fransson, Phys. Rev. Lett. **108**, 057204 (2012).

[20] D. Thonig, Y. Kvashnin, O. Eriksson, and M. Pereiro, Phys. Rev. Mater. **2**, 013801 (2018).

[21] V. Kamberský, Czech. J. Phys. **26**, 1366 (1976).

[22] K. Gilmore, Y. U. Idzerda, and M. D. Stiles, Phys. Rev. Lett. **99**, 027204 (2007).

[23] H. Ebert, S. Mankovsky, D. Ködderitzsch, and P. J. Kelly, Phys. Rev. Lett. **107**, 066603 (2011).

[24] S. Brinker, M. dos Santos Dias, and S. Lounis, J. Phys.: Condens. Matter **34**, 285802 (2022).

[25] T. Weindler, H. G. Bauer, R. Islinger, B. Boehm, J.-Y. Chauleau, and C. H. Back, Phys. Rev. Lett. **113**, 237204 (2014).

[26] V. Bar'yakhtar, Sov. Phys. JETP **60**, 863 (1984).

[27] M. Dvornik, A. Vansteenkiste, and B. Van Waeyenberge, Phys. Rev. B **88**, 054427 (2013).

[28] W. Wang, M. Dvornik, M.-A. Bisotti, D. Chernyshenko, M. Beg, M. Albert, A. Vansteenkiste, B. V. Waeyenberge, A. N. Kuchko, V. V. Kruglyak *et al.*, Phys. Rev. B **92**, 054430 (2015).

[29] Z. Ma and D. G. Seiler, *Metrology and Diagnostic Techniques for Nanoelectronics* (Jenny Stanford Publishing, New York, 2017).

[30] W. Zhu, Z. Zhu, D. Li, G. Wu, L. Xi, Q. Jin, and Z. Zhang, J. Magn. Magn. Mater. **479**, 179 (2019).

[31] R. Urban, G. Woltersdorf, and B. Heinrich, Phys. Rev. Lett. **87**, 217204 (2001).

[32] M. A. Schoen, D. Thonig, M. L. Schneider, T. Silva, H. T. Nembach, O. Eriksson, O. Karis, and J. M. Shaw, Nat. Phys. **12**, 839 (2016).

[33] C. Etz, L. Bergqvist, A. Bergman, A. Taroni, and O. Eriksson, J. Phys.: Condens. Matter **27**, 243202 (2015).

[34] Y. Nambu, J. Barker, Y. Okino, T. Kikkawa, Y. Shiomi, M. Enderle, T. Weber, B. Winn, M. Graves-Brook, J. M. Tranquada, T. Ziman, M. Fujita, G. E. W. Bauer, E. Saitoh, and K. Kakurai, Phys. Rev. Lett. **125**, 027201 (2020).

[35] T. Balashov, A. F. Takács, M. Däne, A. Ernst, P. Bruno, and W. Wulfhekel, Phys. Rev. B **78**, 174404 (2008).

[36] T. Balashov, P. Buczek, L. Sandratskii, A. Ernst, and W. Wulfhekel, J. Phys.: Condens. Matter **26**, 394007 (2014).

[37] A. T. Costa, R. B. Muniz, S. Lounis, A. B. Klautau, and D. L. Mills, Phys. Rev. B **82**, 014428 (2010).

[38] H. J. Qin, K. Zakeri, A. Ernst, T.-H. Chuang, Y.-J. Chen, Y. Meng, and J. Kirschner, Phys. Rev. B **88**, 020404(R) (2013).

[39] A. Chakraborty, P. Wenk, and J. Schliemann, Eur. Phys. J. B **88**, 64 (2015).

[40] Y. Zhang, T.-H. Chuang, K. Zakeri, J. Kirschner *et al.*, Phys. Rev. Lett. **109**, 087203 (2012).

[41] J. Mentink, M. Tretyakov, A. Fasolino, M. Katsnelson, and T. Rasing, J. Phys.: Condens. Matter **22**, 176001 (2010).

[42] A. Brataas, Y. Tserkovnyak, and G. E. W. Bauer, Phys. Rev. B **84**, 054416 (2011).

[43] C. Vittoria, S. D. Yoon, and A. Widom, Phys. Rev. B **81**, 014412 (2010).

[44] E. Rossi, O. G. Heinonen, and A. H. MacDonald, Phys. Rev. B **72**, 174412 (2005).

[45] A. Rückriegel and P. Kopietz, Phys. Rev. Lett. **115**, 157203 (2015).

[46] D. Thonig, J. Henk, and O. Eriksson, Phys. Rev. B **92**, 104403 (2015).

[47] Uppsala atomistic spin dynamics (UppASD) code available under gnu general public license, http://physics.uu.se/uppasd and http://github.com/UppASD/UppASD.

[48] A. Bergman, A. Taroni, L. Bergqvist, J. Hellsvik, B. Hjörvarsson, and O. Eriksson, Phys. Rev. B **81**, 144416 (2010).

[49] M. Mourigal, M. E. Zhitomirsky, and A. L. Chernyshev, Phys. Rev. B **82**, 144402 (2010).

[50] J. Kübler, *Theory of Itinerant Electron Magnetism* (Oxford University Press, Oxford, 2017), Vol. 106.

[51] S. V. Halilov, H. Eschrig, A. Y. Perlov, and P. M. Oppeneer, Phys. Rev. B **58**, 293 (1998).

[52] H. J. Skadsem, Y. Tserkovnyak, A. Brataas, and G. E. W. Bauer, Phys. Rev. B **75**, 094416 (2007).

[53] S. Mankovsky, S. Wimmer, and H. Ebert, Phys. Rev. B **98**, 104406 (2018).

[54] W. Marshall and R. D. Lowde, Rep. Prog. Phys. **31**, 705 (1968).

[55] P. R. Peduto, S. Frota-Pessoa, and M. S. Methfessel, Phys. Rev. B **44**, 13283 (1991).

[56] S. Frota-Pessoa, Phys. Rev. B **46**, 14570 (1992).

[57] R. Haydock, *Solid State Physics* (Elsevier, Amsterdam, 1980), Vol. 35, pp. 215–294.

[58] N. Beer and D. Pettifor, *The Electronic Structure of Complex Systems* (Springer, New York, 1984), pp. 769–777.

[59] O. K. Andersen, Phys. Rev. B **12**, 3060 (1975).

[60] S. Frota-Pessôa, R. B. Muniz, and J. Kudrnovský, Phys. Rev. B **62**, 5293 (2000).

[61] S. Frota-Pessôa, Phys. Rev. B **69**, 104401 (2004).

[62] U. von Barth and L. Hedin, J. Phys. C **5**, 1629 (1972).

[63] J. P. Perdew, K. Burke, and M. Ernzerhof, Phys. Rev. Lett. **77**, 3865 (1996).

[64] O. Eriksson, B. Johansson, R. C. Albers, A. M. Boring, and M. S. S. Brooks, Phys. Rev. B **42**, 2707 (1990).

[65] I. Ohnuma, H. Enoki, O. Ikeda, R. Kainuma, H. Ohtani, B. Sundman, and K. Ishida, Acta Mater. **50**, 379 (2002).

[66] *American Institute of Physics Handbook*, 3rd ed., edited by B. H. Billins and D. E. Gray (McGraw-Hill, New York, 1972).

[67] H. P. Wijn, *Magnetic Properties of Metals: D-elements, Alloys and Compounds* (Springer Science & Business Media, Berlin, 1991).

[68] T. Burkert, L. Nordström, O. Eriksson, and O. Heinonen, Phys. Rev. Lett. **93**, 027203 (2004).

[69] M. Mašín, L. Bergqvist, J. Kudrnovský, M. Kotrla, and V. Drchal, Phys. Rev. B **87**, 075452 (2013).

[70] P. Söderlind, O. Eriksson, B. Johansson, R. C. Albers, and A. M. Boring, Phys. Rev. B **45**, 12911 (1992).

[71] A. Bergman and O. Eriksson, Phys. Rev. B **74**, 104422 (2006).

[72] A. Díaz-Ortiz, R. Drautz, M. Fähnle, H. Dosch, and J. M. Sanchez, Phys. Rev. B **73**, 224208 (2006).

[73] J. P. Trinastic, Y. Wang, and H.-P. Cheng, Phys. Rev. B **88**, 104408 (2013).

[74] K. M. Seemann, F. Freimuth, H. Zhang, S. Blügel, Y. Mokrousov, D. E. Bürgler, and C. M. Schneider, Phys. Rev. Lett. **107**, 086603 (2011).

[75] J. Lourembam, K. H. Khoo, J. Qiu, H. Xie, S. K. Wong, Q. J. Yap, and S. T. Lim, Adv. Electron. Mater. **7**, 2100351 (2021).

[76] S. Mankovsky, D. Ködderitzsch, G. Woltersdorf, and H. Ebert, Phys. Rev. B **87**, 014430 (2013).

[77] I. Turek, J. Kudrnovský, and V. Drchal, Phys. Rev. B **92**, 214407 (2015).

[78] I. P. Miranda, A. B. Klautau, A. Bergman, D. Thonig, H. M. Petrilli, and O. Eriksson, Phys. Rev. B **103**, L220405 (2021).

[79] J. M. Shaw, R. Knut, A. Armstrong, S. Bhandary, Y. Kvashnin, D. Thonig, E. K. Delczeg-Czirjak, O. Karis, T. J. Silva, E. Weschke, H. T. Nembach, O. Eriksson, and D. A. Arena, Phys. Rev. Lett. **127**, 207201 (2021).

[80] I. Garate and A. MacDonald, Phys. Rev. B **79**, 064403 (2009).

[81] A. I. Liechtenstein, M. Katsnelson, V. Antropov, and V. Gubanov, J. Magn. Magn. Mater. **67**, 65 (1987).

[82] A. Zunger, S.-H. Wei, L. G. Ferreira, and J. E. Bernard, Phys. Rev. Lett. **65**, 353 (1990).

[83] A. van de Walle, P. Tiwary, M. de Jong, D. Olmsted, M. Asta, A. Dick, D. Shin, Y. Wang, L.-Q. Chen, and Z.-K. Liu, Calphad **42**, 13 (2013).

[84] M. Hoffmann, A. Ernst, W. Hergert, V. N. Antonov, W. A. Adeagbo, R. M. Geilhufe, and H. Ben Hamed, Phys. Status Solidi B **257**, 1900671 (2020).

[85] M. Pajda, J. Kudrnovský, I. Turek, V. Drchal, and P. Bruno, Phys. Rev. B **64**, 174402 (2001).

[86] A. A. Starikov, P. J. Kelly, A. Brataas, Y. Tserkovnyak, and G. E. W. Bauer, Phys. Rev. Lett. **105**, 236601 (2010).
[87] D. Bardos, J. Appl. Phys. **40**, 1371 (1969).
[88] M. Oogane, T. Wakitani, S. Yakata, R. Yilgin, Y. Ando, A. Sakuma, and T. Miyazaki, Jpn. J. Appl. Phys. **45**, 3889 (2006).
[89] B. Khodadadi, A. Rai, A. Sapkota, A. Srivastava, B. Nepal, Y. Lim, D. A. Smith, C. Mewes, S. Budhathoki, A. J. Hauser, M. Gao, J.-F. Li, D. D. Viehland, Z. Jiang, J. J. Heremans, P. V. Balachandran, T. Mewes, and S. Emori, Phys. Rev. Lett. **124**, 157201 (2020).
[90] C. Scheck, L. Cheng, I. Barsukov, Z. Frait, and W. E. Bailey, Phys. Rev. Lett. **98**, 117601 (2007).
[91] S. M. Bhagat and P. Lubitz, Phys. Rev. B **10**, 179 (1974).
[92] Y. Hsu and L. Berger, Phys. Rev. B **18**, 4856 (1978).
[93] M. A. W. Schoen, J. Lucassen, H. T. Nembach, B. Koopmans, T. J. Silva, C. H. Back, and J. M. Shaw, Phys. Rev. B **95**, 134411 (2017).
[94] A. J. Lee, J. T. Brangham, Y. Cheng, S. P. White, W. T. Ruane, B. D. Esser, D. W. McComb, P. C. Hammel, and F. Yang, Nat. Commun. **8**, 234 (2017).
[95] Y. Zhao, Y. Liu, H. Tang, H. Jiang, Z. Yuan, and K. Xia, Phys. Rev. B **98**, 174412 (2018).
[96] P. Karipoth, A. Thirumurugan, and R. J. Joseyphus, J. Colloid Interface Sci. **404**, 49 (2013).
[97] Y. Li, F. Zeng, S. S.-L. Zhang, H. Shin, H. Saglam, V. Karakas, O. Ozatay, J. E. Pearson, O. G. Heinonen, Y. Wu, A. Hoffmann, and W. Zhang, Phys. Rev. Lett. **122**, 117203 (2019).
[98] P. Karipoth, A. Thirumurugan, S. Velaga, J.-M. Greneche, and R. Justin Joseyphus, J. Appl. Phys. **120**, 123906 (2016).
[99] X. Liu, M. M. Steiner, R. Sooryakumar, G. A. Prinz, R. F. C. Farrow, and G. Harp, Phys. Rev. B **53**, 12166 (1996).
[100] J. Walowski, M. D. Kaufmann, B. Lenk, C. Hamann, J. McCord, and M. Münzenberg, J. Phys. D **41**, 164016 (2008).
[101] B. Heinrich, D. Meredith, and J. Cochran, J. Appl. Phys. **50**, 7726 (1979).
[102] N. Umetsu, D. Miura, and A. Sakuma, J. Phys. Soc. Jpn. **81**, 114716 (2012).
[103] X. Z. Chen, R. Zarzuela, J. Zhang, C. Song, X. F. Zhou, G. Y. Shi, F. Li, H. A. Zhou, W. J. Jiang, F. Pan, and Y. Tserkovnyak, Phys. Rev. Lett. **120**, 207204 (2018).
[104] F. Mahfouzi and N. Kioussis, Phys. Rev. B **98**, 220410(R) (2018).
[105] H. A. Mook and D. M. Paul, Phys. Rev. Lett. **54**, 227 (1985).
[106] J. W. Lynn, Phys. Rev. B **11**, 2624 (1975).
[107] C.-K. Loong, J. Carpenter, J. Lynn, R. Robinson, and H. Mook, J. Appl. Phys. **55**, 1895 (1984).
[108] T. Balashov, Inelastic scanning tunneling spectroscopy: Magnetic excitations on the nanoscale, Ph.D. thesis, Karlsruher Institut für Technologie, 2009.
[109] M. Katsnelson and A. Lichtenstein, J. Phys.: Condens. Matter **16**, 7439 (2004).
[110] E. Barati, M. Cinal, D. M. Edwards, and A. Umerski, Phys. Rev. B **90**, 014420 (2014).
[111] X. Wu, Z. Liu, and T. Luo, J. Appl. Phys. **123**, 085109 (2018).
[112] P. Depondt and F. Mertens, J. Phys.: Condens. Matter **21**, 336005 (2009).
[113] M. C. Hickey and J. S. Moodera, Phys. Rev. Lett. **102**, 137601 (2009).
[114] D. van Seters, T. Ludwig, H. Y. Yuan, and R. A. Duine, Dissipation-free modes in dissipative systems, arXiv:2206.07471.
[115] B. Velický, Phys. Rev. **184**, 614 (1969).
[116] R. Chimata, E. K. Delczeg-Czirjak, A. Szilva, R. Cardias, Y. O. Kvashnin, M. Pereiro, S. Mankovsky, H. Ebert, D. Thonig, B. Sanyal, A. B. Klautau, and O. Eriksson, Phys. Rev. B **95**, 214417 (2017).
[117] M. Oogane, T. Kubota, H. Naganuma, and Y. Ando, J. Phys. D **48**, 164012 (2015).
[118] I. Turek, J. Kudrnovský, V. Drchal, and P. Weinberger, Phys. Rev. B **49**, 3352 (1994).
[119] F. S. Guimaraes, J. R. Suckert, J. Chico, J. Bouaziz, M. dos Santos Dias, and S. Lounis, J. Phys.: Condens. Matter **31**, 255802 (2019).
[120] Z. Yuan, K. M. D. Hals, Y. Liu, A. A. Starikov, A. Brataas, and P. J. Kelly, Phys. Rev. Lett. **113**, 266603 (2014).
[121] A. Sakuma, J. Appl. Phys. **117**, 013912 (2015).